Gravity Anomalies of the Ridge-Transform System in the South Atlantic Between 31 and 34.5° S: Upwelling Centers and Variations in Crustal Thickness

BAN-YUAN KUO and DONALD W. FORSYTH
Department of Geological Sciences, Brown University, Providence, Rhode Island 02912, U.S.A.

(Received 7 March, 1988)

Key words: Gravity anomalies, Ridge-transform system, Mantle upwelling, Crustal thickness.

Abstract. To decipher the distribution of mass anomalies near the earth's surface and their relation to the major tectonic elements of a spreading plate boundary, we have analyzed shipboard gravity data in the vicinity of the southern Mid-Atlantic Ridge at 31–34.5° S. The area of study covers six ridge segments, two major transforms, the Cox and Meteor, and three small offsets or discordant zones. One of these small offsets is an elongate, deep basin at 33.5° S that strikes at about 45° to the adjoining ridge axes.

By subtracting from the free-air anomaly the three-dimensional (3-D) effects of the seafloor topography and Moho relief, assuming constant densities of the crust and mantle and constant crustal thickness, we generate the mantle Bouguer anomaly. The mantle Bouguer anomaly is caused by variations in crustal thickness and the temperature and density structure of the mantle. By subtracting from the mantle Bouguer anomaly the effects of the density variations due to the 3-D thermal structure predicted by a simple model of passive flow in the mantle, we calculate the residual gravity anomalies. We interpret residual gravity anomalies in terms of anomalous crustal thickness variations and/or mantle thermal structures that are not considered in the forward model. As inferred from the residual map, the deep, major fracture zone valleys and the median, rift valleys are not isostatically compensated by thin crust. Thin crust may be associated with the broad, inactive segment of the Meteor fracture zone but is not clearly detected in the narrow, active transform zone. On the other hand, the presence of high residual anomalies along the relict trace of the oblique offset at 33.5° S suggests that thin crust may have been generated at an oblique spreading center which has experienced a restricted magma supply. The two smaller offsets at 31.3° S and 32.5° S also show residual anomalies suggesting thin crust but the anomalies are less pronounced than that at the 33.5° S oblique offset. There is a distinct, circular-shaped mantle Bouguer low centered on the shallowest portion of the ridge segment at about 33° S, which may represent upwelling in the form of a mantle plume beneath this ridge, or the progressive, along-axis crustal thinning caused by a centered, localized magma supply zone. Both mantle Bouguer and residual anomalies show a distinct, local low to the west of the ridge south of the 33.5° S oblique offset and relatively high values at and to the east of this ridge segment. We interpret this pattern as an indication that the upwelling center in the mantle for this ridge is off-axis to the west of the ridge.

1. Introduction

During the cruises Marathon 10 and 13 aboard the R/V *Thomas Washington* in December 1984 and April 1985, SeaBeam topography, gravity, and magnetic data were collected at the Mid-Atlantic Ridge (MAR) between 31 and 34.5° S. This is one of the first times that a detailed geophysical survey has been carried out for this long, but relatively unknown, accreting plate boundary. The magnetic anomaly pattern reveals that the ridge at this latitude is spreading at a full rate of about 35–40 mm yr^{-1} (Welch *et al.*, 1987).

As one approach to studying the tectonics of spreading centers, the gravity data collected from these cruises are analyzed in this paper to investigate the variation in crustal thickness of the ridge-transform system in this area. Understanding the crustal structure will help delineate the relationships of magma supply, crustal deformation, ridge offsets, and dynamic processes in the mantle. Local, detailed crustal structure can typically be retrieved from seismic refraction experiments, most of which have been designed to determine the seismic velocities and layering of the oceanic crust along the shot line (e.g., Detrick and Purdy, 1980). Gravity data, despite missing detailed depth resolution, provides an efficient means of mapping lateral variations in crustal structure on a regional scale. Recently, Prince and Forsyth (1988) applied three-dimensional (3-D) analysis techniques to model the gravity anomaly at the intersection of the northern MAR and the Vema

Marine Geophysical Researches **10**: 205–232, 1988.

fracture zone. The gravity modelling allowed them to infer the horizontal extent of the thin crust beneath the Vema transform, and the distribution of thin crust was confirmed by refraction profiles crossing the transform (Detrick *et al.*, 1982; Louden *et al.*, 1986). This gives us confidence that the 3-D modelling technique can adequately resolve the crustal information from the observed gravity data, at least for areas of simple ridge-transform geometry like the Vema-MAR intersection. Unlike some North Atlantic ridges and transforms, there is no seismic refraction data available for the southern MAR which can be compared with the results of the gravity analysis. This study thus gives a regional estimate of the characteristics of the crustal thickness variation and type of isostasy along one section of the southern MAR, and helps find interesting points for further detailed exploration. We first briefly review the morphology of the tectonic elements. Then we present our gravity data and methodology of the 3-D modelling. Last, we interpret the analyzed gravity data in terms of anomalous crustal thickness and/or mantle thermal structure.

2. Ridge-Transform Morphology

The region that our gravity data covers extends from about 31 to 34.5° S, and from 12.5 to 15.5° W. Fox *et al.* (1989) summarize the tectonic setting and history of this area. In this paper, we process the observed data in a rotated coordinate system within a rectangular region of 256 km by 512 km that covers effectively all the useful bathymetry and gravity data. Figure 1 sketches the geometric configuration of the important tectonic elements in the rotated map, and we will show all the subsequent analyzed data in the same map. We construct the bathymetry map from the SeaBeam bathymetry data of Nishimura and Forsyth (1988). The navigation in their data set has been improved by deriving a smooth function describing the ship's position that attempts to minimize the SeaBeam crossing errors, matching the optimum position within a root-mean-square (RMS) error of about 200 meters. We interpolated the SeaBeam data into grids spaced at 1 km in the map area using a 2-D gaussian averaging curve with cut-off distance equal to the grid spacing and fall-off distance equal to half the spacing. This left gaps at points more than 1 km away from the outer beam of the SeaBeam swath. The gaps were then filled by interpolating and extrapolating from the SeaBeam-controlled points based on the minimum curvature criterion (Briggs, 1974). The final bathymetry map at spatial resolution 1 km is shown in Figure 2. The bathymetry in the central portion of the map is well constrained by the real SeaBeam data because each SeaBeam track is 2–2.5 km wide on average and the tracks with the SeaBeam data are even denser than those with the gravity data shown in Figure 3. Away from the SeaBeam tracks, the minimum curvature algorithm returns the predicted depth to the local average level. Figures 1 and 2 show that the ridge-transform (RT) system consists of six ridge segments (numbered in Figure 1), two major transform faults, and three smaller offsets separating the ridge segments. Neither the ridge segments nor the transforms exhibit consistent morphology. Ridge segments 2 and 5 appear to have rift valleys 1–1.5 km deep that are typical of the slow-spreading, northern MAR. In contrast, the very shallow, subtle median valley near the middle of ridge segment 4 is similar to the ridge topography of the intermediate-fast spreading East Pacific Rise (EPR), but it gradually deepens to a pronounced rift valley near the ends of the segment.

The two transforms also show markedly different morphologies. The 95 km long Cox transform consists of two parallel, straight escarpments which define the boundaries of a 10 km wide, deep trough of complexly disturbed topography. The tectonic evolution of this transform is not known at present, but its morphologic character resembles many major transforms that are composed of two strike-slip faults linked by an 'extensional relay zone', such as the Tamayo (Macdonald *et al.*, 1979), Rivera (Prothero and Reid, 1982), Orozco (Trehu and Solomon, 1983), and Siqueiros (Crane, 1976) transforms on the EPR, and the Gibbs transform on the northern MAR (Searle, 1981). We recognize the Cox transform as a similar type of double transform, although the exact position of the current relay zone or zones is not known because there is a series of deformed, deep basins instead of a simple, orthogonal rift basin. Much of the seafloor within the inactive Cox fracture zone valley, however, has a lineated fabric semi-orthogonal to the transform, suggesting that it was created at a simple rifting center. In contrast, the Meteor transform (70 km long) has a very narrow

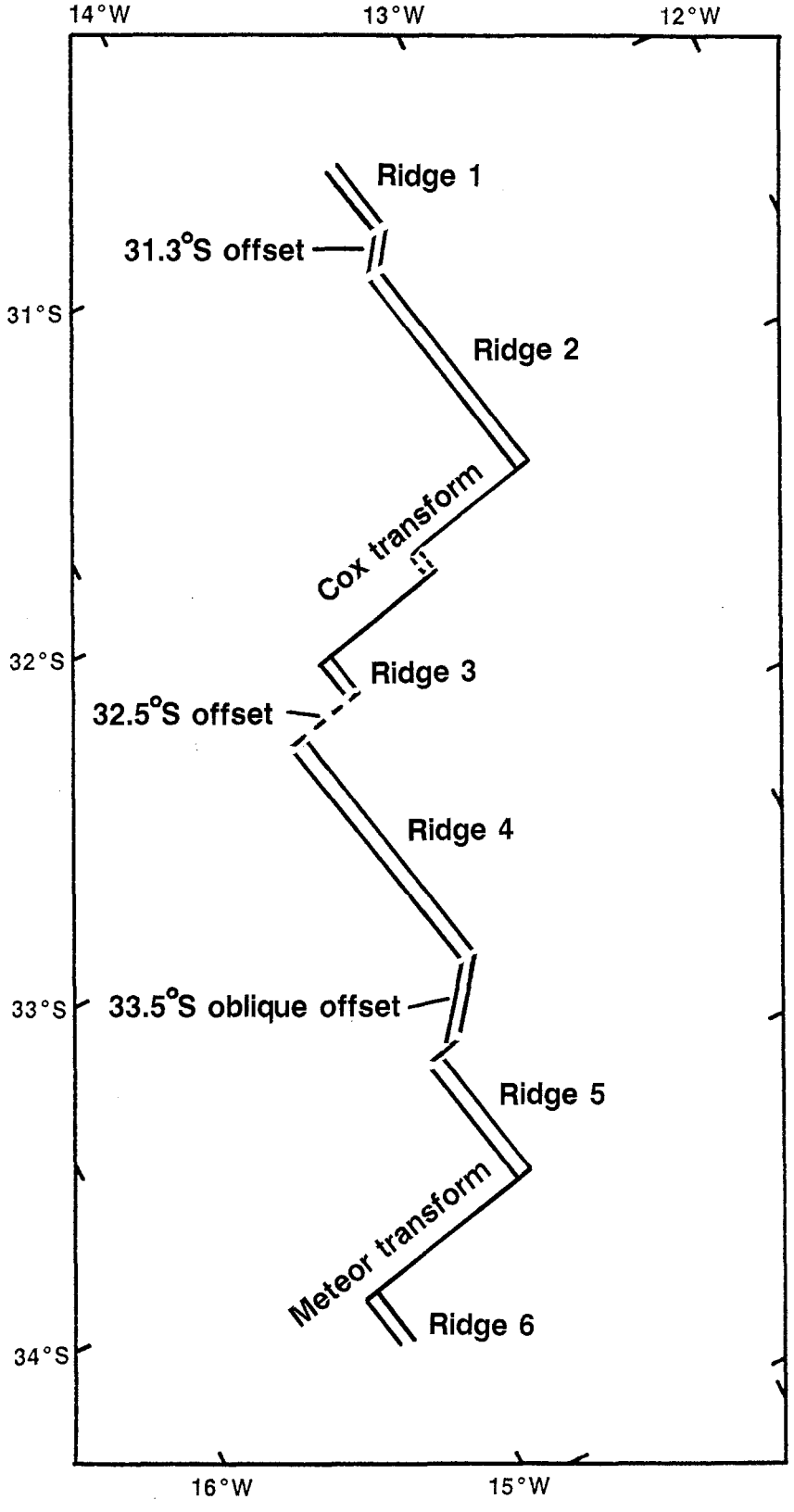

Fig. 1. First-order plate boundary map of the study area. The upper-left corner of the map is 30.18° S, 14.14° W and the edges of the map are rotated about 26° relative to the local latitude and longitude lines. The same map area is used for other figures. The six ridge segments from north to south, two major transforms and three small offsets or discordant zones are labeled.

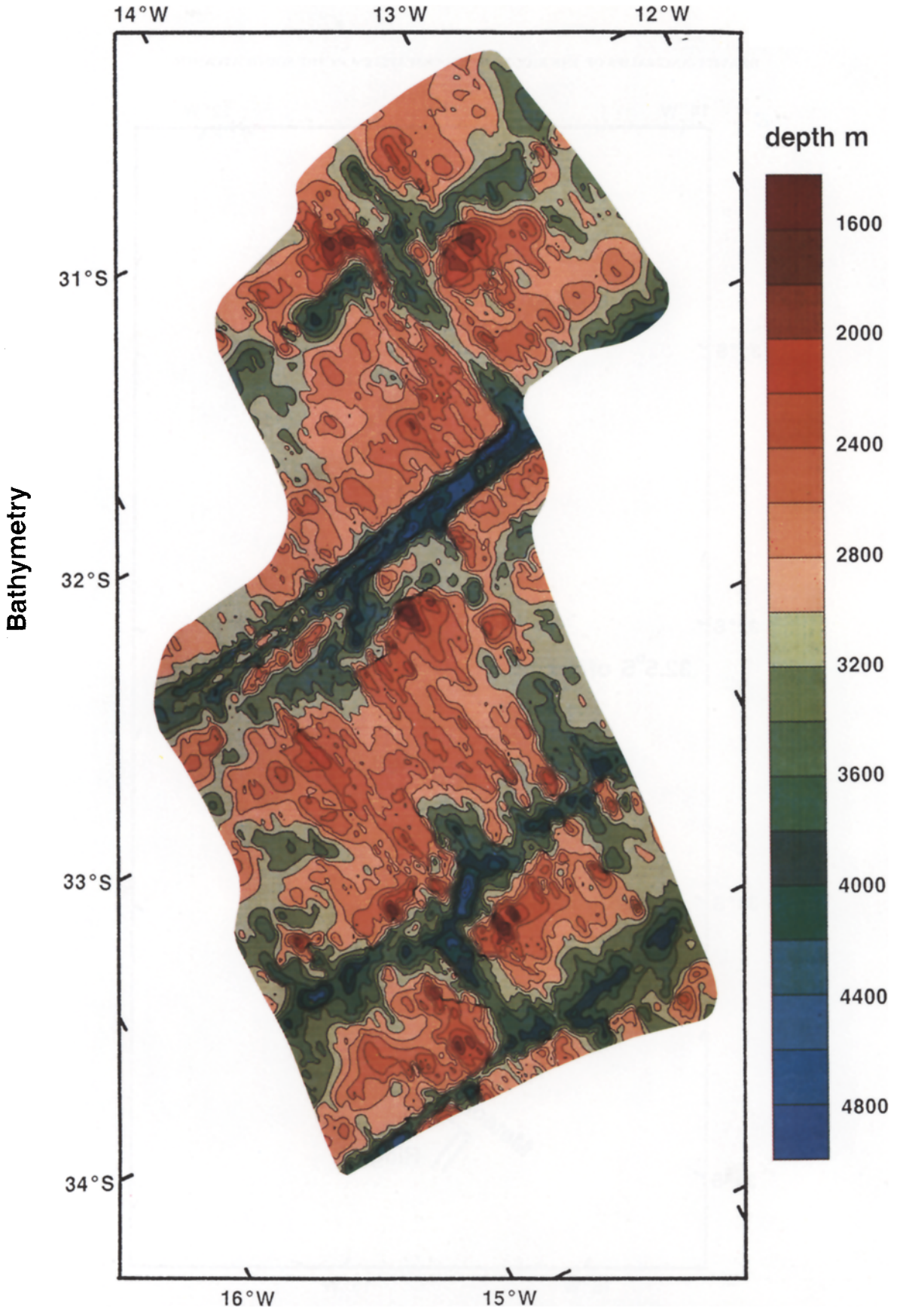

Fig. 2. Bathymetric map of the entire survey area. SeaBeam coverage is more extensive than the gravity coverage shown in Figure 3, since many short segments were eliminated in the gravity compilation (there were 751 crossings of tracklines in the SeaBeam data set as opposed to 360 in the gravity set). Map is machine contoured on a 1-km grid with values at grid points between SeaBeam swaths generated by an algorithm based on the minimum curvature criterion.

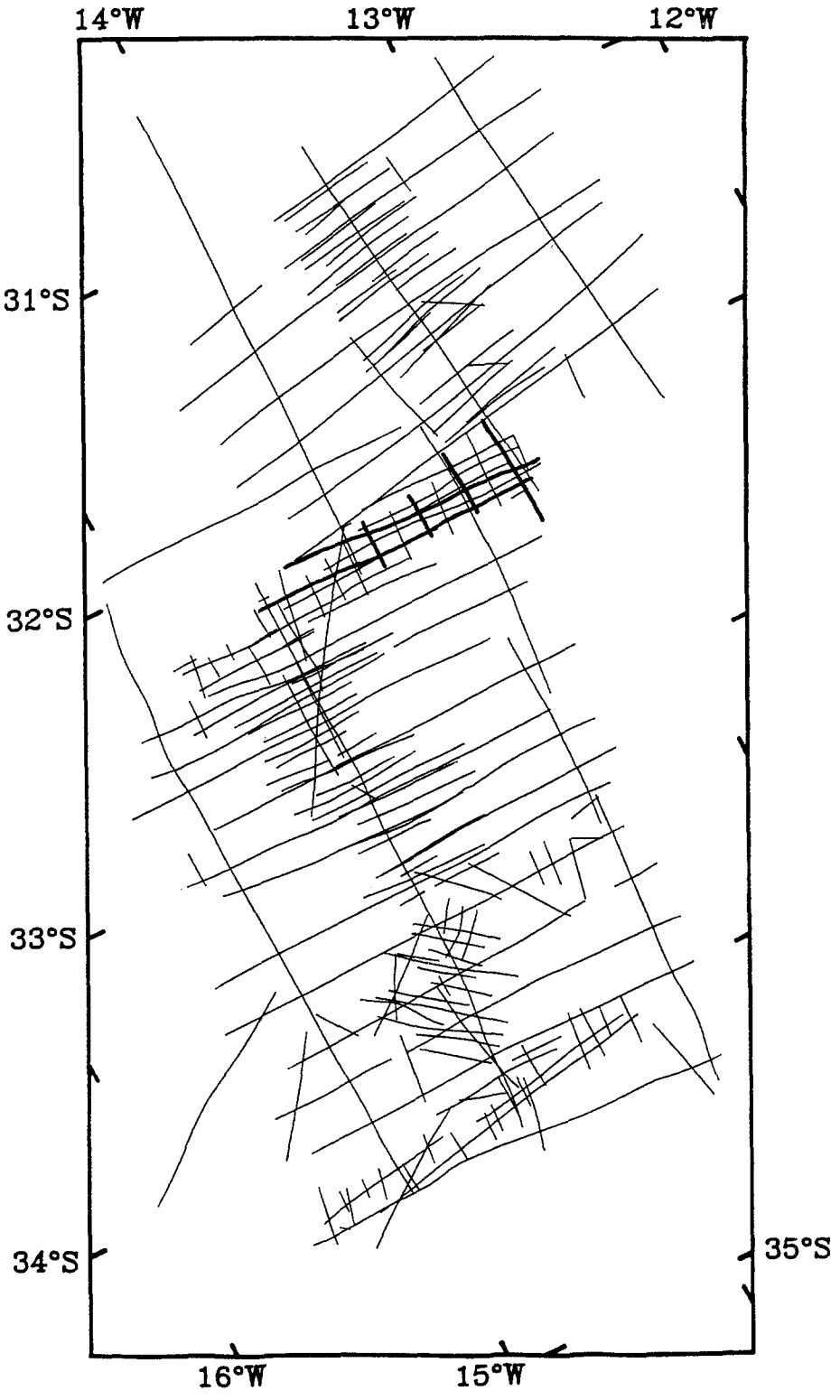

Fig. 3. Ship track segments in the survey area on which the gravity data are of acceptable quality. Each track segment crosses at least one other track with acceptable data. Note that all data are interlinked. Thick lines indicate profiles shown in Figure 11.

trough of simple internal geometry similar to the Kane transform in the Northern Atlantic (e.g., Pochalny *et al.*, 1988). The narrow trough widens into a broad depression in the inactive fracture zone to the east. The triangular-shaped nodal basin that is common at the North Atlantic RT intersections can be observed at the western intersection of the Meteor transform, but it may be either absent or considerably deformed at other intersections in this area. Possible relict nodal basins are also recognized along the Meteor fracture zone, such as at 34.2° S, 14.7° W.

The three small offsets interrupt the ridge segments at approximately 31.3° S, 32.5° S, and 33.5° S, respectively. The most remarkable among them is the last one which is in the shape of an elongate deep basin trending at about 45° with respect to the adjoining ridge segment 4 to the north and ridge segment 5 to the south and displaces the two ridges by 25 km (Figures 1 and 2). On both the west and east sides of this oblique basin, fracture zone traces that are characterized by ridge-perpendicular morphological grain can be identified. These two traces appear to extend from the two tips of the adjoining ridge segments and are not aligned in one line. The magnetic anomalies (Welch *et al.*, 1987) reveal that, between 3.4 and 1.7 Ma, ridge segment 4 had an average spreading rate of 16 km m.y.$^{-1}$ to the west and 18 km m.y.$^{-1}$ to the east, and ridge segment 5 had an average spreading rate of 21 km m.y.$^{-1}$ to the west and 11 km m.y.$^{-1}$ to the east (These numbers are independent estimates for each ridge segment and have not been adjusted to sum to a constant rate). The length of the offset between the two ridges decreased by about 10 km during this period. We infer that the current oblique offset has evolved from a transform fault, but the cause of the non-orthogonality of the offset relative to the ridge is not as clear. As a result of its oblique orientation, there must be a substantial component of spreading on the offset, which might best be described as an oblique spreading center. The northernmost small offset at 31.3° S is about 14 km long. Magnetic anomalies show that between 3.9 and 2.5 Ma it increased in length by about 6 km to its current geometry (Welch *et al.*, 1987). The offset at 32.5° S connects ridge segment 4 and the short (10 km) ridge 2 abutting the Cox transform to the north. There is no magnetic data available for this offset, but the morphologic fabric 50 km to the west shows obvious signs of disturbance, suggesting that the offset has been active for at least 2.5 m.y.

3. Free-Air Anomaly and the Methodology

In the construction of a free-air anomaly (FAA) map, it is essential to reconcile the crossover errors between ship tracks. Crossover errors are primarily due to incorrect calibration of the gravimeter at ports, navigation errors, non-linear drift of the instrument, and cross-coupling errors in the gravimeter (Talwani, 1966; Prince and Forsyth, 1984; Weissel and Watts, 1988). Although we used improved navigation data, raw crossover errors of the gravity data were still large. In this survey, there was clearly an incorrect tie to the base station in at least one port, probably in two. We first subtracted an apparent linear drift with time caused by incorrect calibration which was inferred from the fact that initial crossover errors increased in proportion to the time separation between the two tracks involved in the crossing. Then we employed the method of Prince and Forsyth (1984) to minimize the crossover errors in a least-squares sense by shifting the FAA on each approximately straight trackline segment by a constant value. The ship tracks with useful gravity data are shown in Figure 3. Only those segments which cross at least one other segment are retained and all segments are interconnected. Many short segments with good SeaBeam data are eliminated either because they do not cross other segments or because it takes roughly 20 min. for the gravimeter to stabilize after a course change. There are in total 360 crossover errors as data and zero levels of 129 track segments as parameters in the inverse problem. After this correction, the RMS value of the corrected crossover errors is 4.5 mgal, and the estimated standard deviation of the errors is 5.7 mgal. These two numbers, although representing a 90% reduction in variance from the unprocessed FAA, are significantly larger than the corresponding 2.9 and 3.8 mgal derived by Prince and Forsyth (1984) in a survey near the Vema Fracture Zone which was processed in the same way. Statistically, any variation greater than 12 mgal can be regarded as real at the 95% confidence level, but extra caution will be taken in our interpretation.

The relatively large crossover error of our adjusted data set probably results from bad weather in sur-

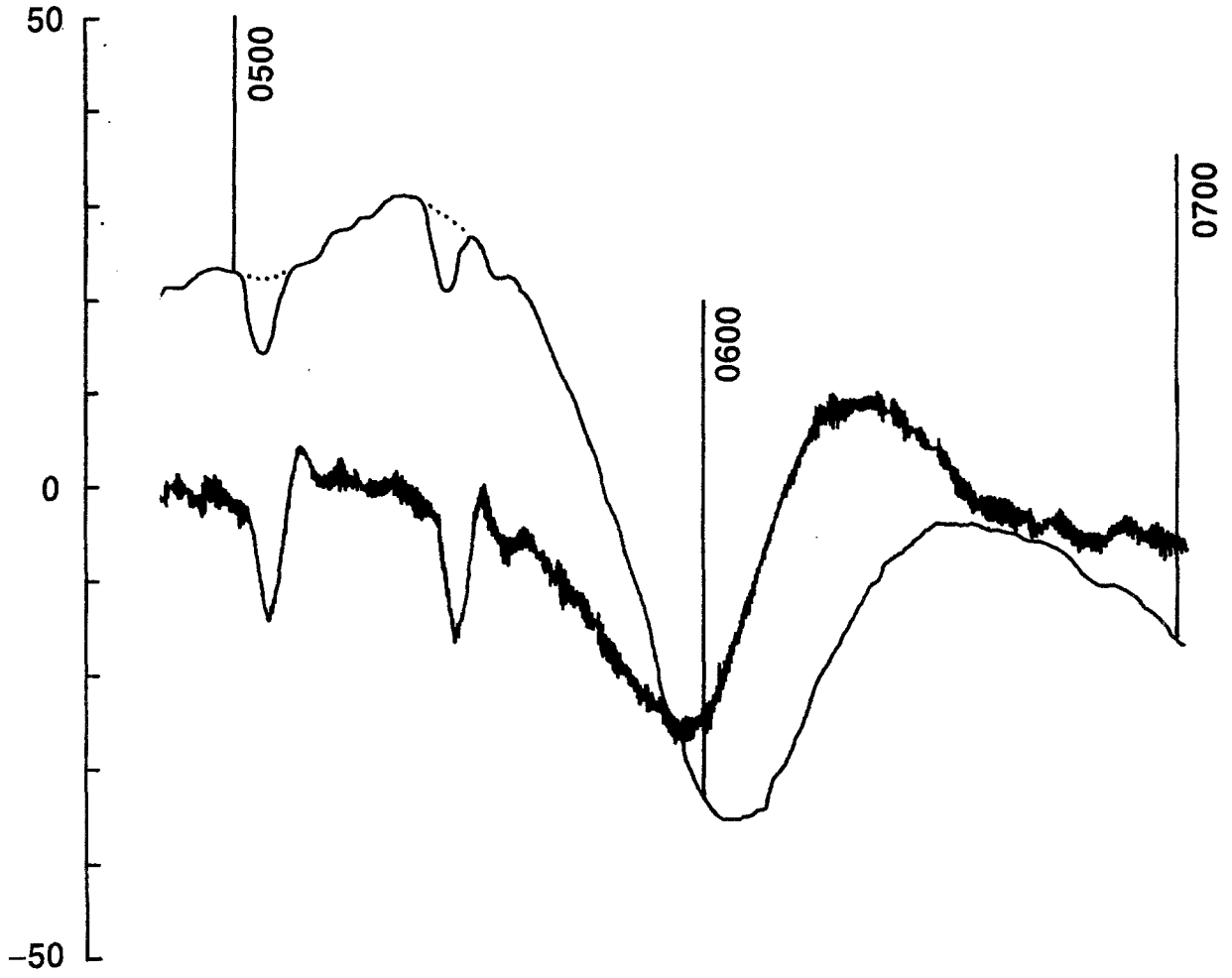

Fig. 4. A small section of the analog gravity record (roughly a 2-hour period) that shows typical mechanical transients or 'glitches' on the two recording components of the gravimeter, the beam position (thicker trace) and the screw position (thinner trace). The gravity data are converted from the position of the screw. The dashed line represents the hand-correction made which traces the signal through the glitch as though it were not present. See text for explanation.

veying along some of the long N-S lines and the occasional instability of the 30-year-old Graf Askania 2 gravimeter. Figure 4 shows an example of the analog recording of the occasional 'glitches' or mechanical transients in the gravimeter that deteriorate the quality of the data. The glitch has a typical width of about 10 minutes, which corresponds to about 3–4 km survey distance. Glitches are recognized on both the 'beam' and 'screw' traces. The beam trace records the deviation of the damped arm of the gravimeter relative to its nominal null position, and the screw trace records the net adjustment that has been made to return the beam to the null position, and thus is indicative of changes in gravitational acceleration. We attempted to correct these glitches by assuming that they are the convolution of an unknown source function with the characteristic response function of the 'beam'. After a series of experiments with chosen, typical glitches, we found that, using a few delta functions with rapidly decreasing amplitude as the source function, the glitches on the 'screw' can be predicted reasonably well and can thus be corrected. In these experiments, however, we found that these corrections are equivalent to bypassing the glitch and connecting the undisturbed signal before and after the glitch smoothly, as illustrated in Figure 4. Since we do not understand the origin of this phenomenom and the result of the correction seems to be logical, we chose to hand-correct the glitches on the 'screw' reading according to our experience from the experiments instead of applying the tedious convolution method to all the glitches in our data set. For typical isolated glitches, correction can be done with confidence. Glitches on

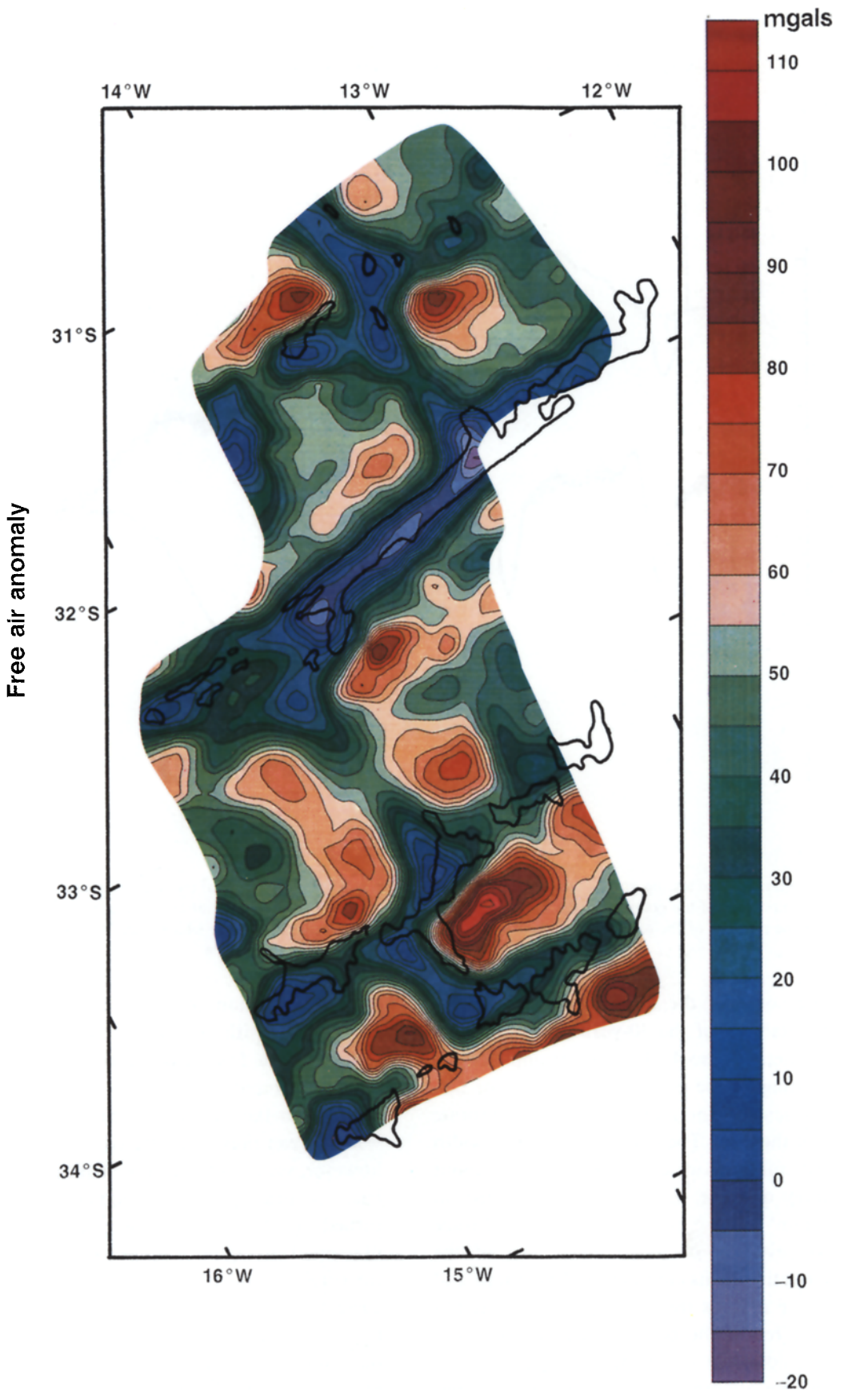

Fig. 5. Free-air anomaly map of the survey area constructed from the data coverage shown in Figure 3 and contoured at 5 mgal intervals. Contours are machine drawn from a grid with 8 km spacing with values generated by a smoothing algorithm (see text). Zero level is arbitrary due to problems with tie-ins at ports. Thick lines are 3600-m bathymetric contours. The 3600-m contours outline primarily the deep, major tectonic features such as transform valleys and rift valleys.

rapidly varying signals are corrected with less confidence. We discarded data with glitches when the undisturbed signal could not be easily traced. Some crossover points occur where correction has been made with less confidence, which may introduce crossover errors.

To construct the FAA map shown in Figure 5, we interpolate the gravity data on tracklines into 8 km-spaced grids using a 2-D gaussian averaging curve with cut-off distance equal to the grid spacing and fall-off distance equal to half the spacing. Since the crossover-error correction is the correction with respect to one arbitrary trackline and the port calibration was incorrect, the high and low in the FAA map can only be considered in a relative sense. The FAA's on the grid points range from -26 to 115 mgal, with the mean at about 50 mgal. The 5 mgal interval contours on the FAA map primarily delineate the RT morphology as shown in the topographic map in Figure 2. The lowest anomalies occur along the transform valleys, the oblique offset, and the rift valleys. Some local highs occur at topographic highs in the vicinity of RT intersections. This indicates that the topography, or the water/crust interface, is the most important contributor to the FAA.

To gain more meaningful results, we adopt the forward modelling approach of Prince and Forsyth (1988) in that we remove the predictable components from the FAA given proper *a priori* assumptions and attribute the residuals to deviations from these assumptions. The predictable gravity field in the model includes (1) gravity effects from the water/crust interface; (2) gravity effects from crust/mantle interface assuming a constant crustal thickness and density; and (3) gravity effects due to 3-D mantle temperature variations. Any error in this model will contribute to the residual gravity anomaly. The error associated with the seafloor topography is small because the topography is well constrained by the SeaBeam data. Errors due to neglecting sediments are small because nowhere within the study area are sediments thicker than 100 m. We expect that most of the residual anomalies stem from variations in crustal thickness and density, i.e., the deviations from the assumed constant thickness and density for the crust. This expectation is partly motivated by the general experience that thin crust often accompanies transforms in the North Atlantic (White *et al.*, 1984). Nonetheless, we are also alert for variations that possibly represent an unmodelled, anomalous mantle thermal structure. Details of the forward corrections are presented in the following sections.

4. Attraction of the Seafloor Topography and Moho Relief

To predict the gravity effect due to the water/crust interface, we assume the densities of the water and crust to be 1.03 and 2.73 g cm^{-3}(1g cm^{-3} = 1 Mg m^{-3}), respectively. As long as constant crustal thickness is assumed, more realistic density stratification in the crust makes little difference because it is the total contrast between water and mantle that is most important. With a stratified crust increasing in density from 2.4 near the surface to 2.95 g cm^{-3} in layer 3, the predicted anomaly is everywhere less than 1 mgal different from the anomaly predicted for a uniform density of 2.73 g cm^{-3}. We use Parker's (1973) method to convert the topographic relief and the constant density contrast to gravity anomalies. Parker's method involves a Taylor's series expansion of powers of the Fourier transform of the topography. The first three terms of the Taylor's series were retained in our calculation to account for the nonlinear nature of the gravitational attraction of large topographic relief. Adding the fourth term contributes less than 0.1 mgal signal. One of the attractive aspects of Parker's approach is that it allows rapid computation by Fast Fourier Transform (FFT). The completely discretized topography map shown in Figure 2 was used in the FFT calculation. The one km spatial resolution of Figure 2 is accurate enough for the upward continuation in this region because all the points in the map are more than 1 km below sea level. Within 20 km of the edge of the map there is almost no real data and the minimum curvature requirement yields a smoothly varying, more or less constant topography. Since this artificial topography is almost uniform along the edges of the map, we did not need to mirror and fold the map or taper the edges to avoid discontinuities at the boundaries introduced by the periodic asumption of the FFT routine. The only real data that will be damaged if we directly use this unfolded map is the data at the right edge, 1/4 up from the bottom of the map. To keep this data useful, we minimize the edge effect and ensure the across-boundary continuity by assigning

the mirror image of the topography at this spot to the opposite side of the map where there is no real data and merging this mirrored data into the remaining map within a taper between 25 km and 35 km from the edge.

In the estimation of the attraction from the Moho, we assume that the crustal thickness is 6 km and the mantle density is 3.33 g cm^{-3}. Six km is a reasonable, global average value for the oceanic crustal thickness (Spudich and Orcutt, 1980) and any deviation of the average in this area from the assumed value is likely to be small compared to the depth to this interface, so will have little effect on the predicted gravitational attraction. Prince and Forsyth (1988) found that as long as a constant thickness is assumed, more realistic density layering in the crust as suggested by seismic refraction data change the results by only a negligible amount. The gravity signal from the Moho is calculated in the same way as for the seafloor topography except that the source is 6 km deeper and about 3 times smaller in strength.

The addition of the signal from seafloor topography and the signal from the assumed Moho produces a gravity map which describes all the easily predicted effects in and above the oceanic crust. To remove this effect from the FAA, we interpolate the gridded, predicted values onto ship tracks where the FAA was actually measured, and subtract these values from the FAA to generate the 'complete mantle Bouguer anomalies' along ship tracks. In each step, we first calculate the corrected data on ship tracks and then make the map based on these data. The along-track correction instead of the direct map-to-map correction ensures that the artificial signals off the ship tracks on the map will not be accumulated to the next corrected map. However, there is another kind of error which cannot be avoided. In the 3-D Bouguer correction, although most of the correction is based on the real SeaBeam topography, the artifical topography determined by the minimum curvature away from the ship track may deviate from the real topography and introduce artificial error to the calculated Bouguer gravity value on ship tracks. Simple numerical tests using a 2-D, semi-infinite mass sheet indicate that, at the observation level d above the source, the signal drops to 25% of the strongest signal as the observation point shifts to a distance d outside the edge of the semi-infinite sheet. For the average seafloor depth of 3 km, the 25% fall-off distance is about 3 km. In the central area where the ship track coverage is dense, the minimum curvature criterion fills in the data gap under the constraints of two very close SeaBeam swaths. However, some ship tracks away from the important morphologic elements are a few tens of km apart and the extrapolated topography will be out of control over several km from real SeaBeam data. A 100 m error at and beyond a distance of 3 km from ship track will introduce about 1.7 mgal error to the gravity signal along the ship track. Although there is no simple way to assess the error of the artificially extrapolated data, we believe that 3 to 4 (1.7×2) mgals is a reasonable estimate of the error associated with the artificial topography for the ship tracks that are isolated by several tens of km from others. At the Moho, the 25% cut-off distance is about 3 times longer because it is deeper, but the error is on the same order as for the seafloor topography because the density contrast is 3 times smaller. We speculate that in the mantle Bouguer anomaly the worst error for some of the isolated ship tracks can be as large as 8 mgal, but the error for the major RT features is much smaller than this value. Errors at the ends of isolated tracks could be larger because three sides, rather than two sides, lack constraints.

5. Complete Mantle Bouguer Anomalies

The mantle Bouguer anomalies on ship tracks are again interpolated into 8 km-grids using the same scheme as for the FAA map and contoured to construct a complete mantle Bouguer anomaly map (Figure 6). This map represents the gravity field after crust and water have been replaced by rock of mantle density and should reveal sub-seafloor variations in density with no direct topographic effects remaining (As for the FAA map, the zero level is arbitrary). The dominant systematic feature of the mantle Bouguer anomalies is the age-dependence of the anomalies. Prominent lows, outlined by the 10 or 20 mgal contours, are associated with ridge segments 1, 2, and 4, and higher anomalies are on both sides of the ridge. This pattern reflects the density increase in the mantle primarily due to the cooling of the upper mantle with increasing age of the seafloor. Note that there is a correlation between the intensity of the lows along the ridges and the nature of the median valley. The lowest values are along ridge 4,

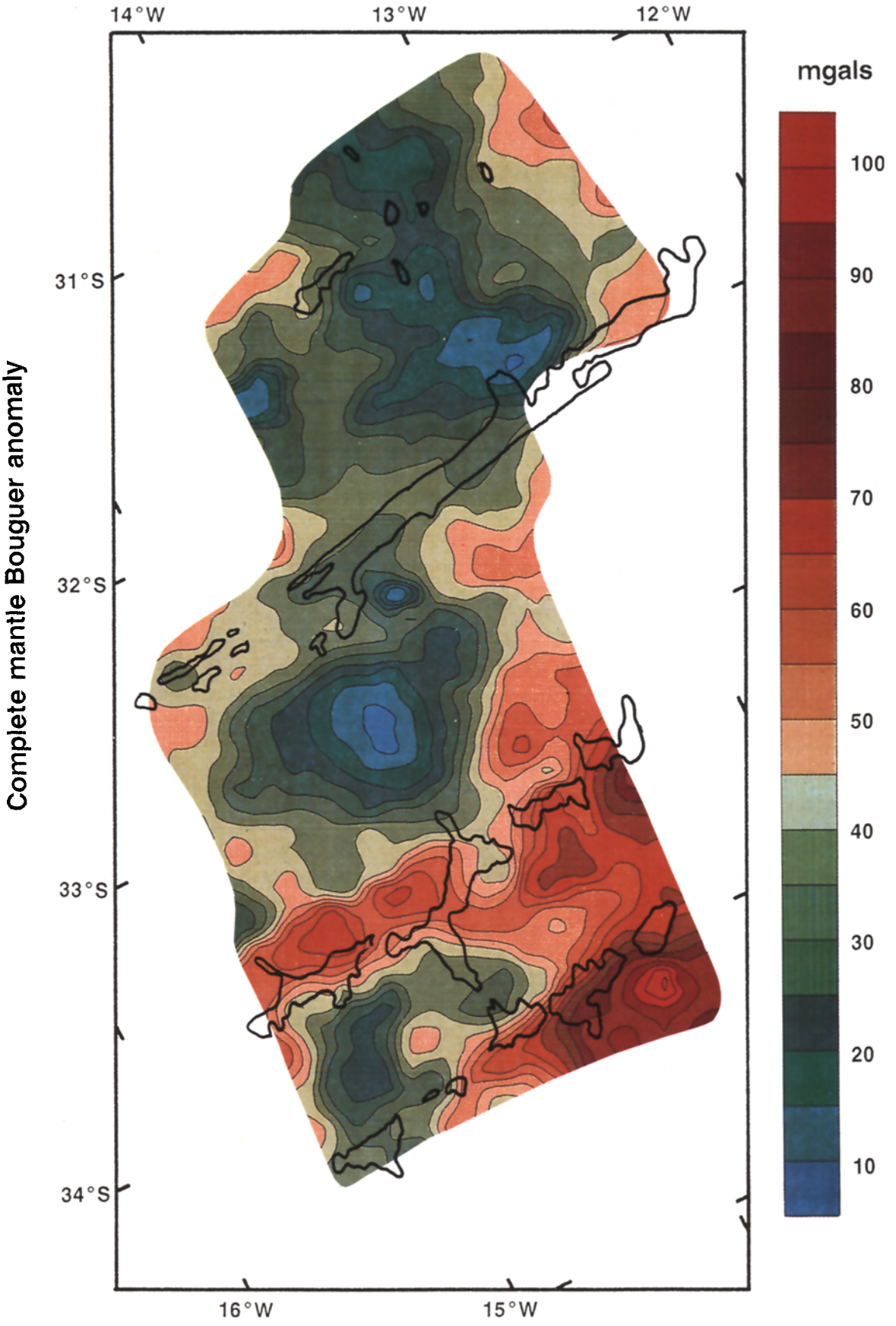

Fig. 6. The mantle Bouguer map contoured at 5 mgal intervals. Mantle Bouguer anomalies are generated by subtracting from the free-air anomaly the attraction of the topography and the attraction of relief on the crust/mantle interface, assuming constant crustal thickness and density. Zero level is arbitrary. 3600-m bathymetric contours are shown to outline the position of fracture zones and rift valleys. Notice that a bulls-eye shaped low anomaly is centered along ridge 4, and a local low is located to the west of ridge 5.

where the median valley largely disappears in the middle of the segment (Figure 2). Ridge segments 1 and 2 have distinct median valleys and a less pronounced low. The mantle Bouguer anomalies along ridge 5 are 20 mgals higher and the median valley is quite deep. The suggestion is that there is a connection between the thermal state of the ridge as revealed in the Bouguer anomalies and the dynamic process of formation of the median valley.

5.1. The bulls-eye pattern

Of particular interest is the pattern of circular contours centered just north of the shallowest portion of ridge 4, in contrast to the elongate lows along ridges 1 and 2 (Figure 6). The circular low could be caused by an along-axis crustal thinning toward both ends of the ridge that is more pronounced and over a longer distance (30–40 km) than along ridge 1 or 2. Or, it could simply indicate that the upwelling of the hot mantle material is more concentrated at the center of ridge 4 than at ridges 1 and 2. Although we cannot separate the variation in crustal thickness from the mantle thermal structure using the gravity anomaly alone, these two effects may not be independent of each other. It has been suggested that the magma needed to form the crust along an entire ridge segment is primarily supplied from a central magma reservoir that is fed by the melt extracted from the upwelling asthenosphere (Whitehead *et al.*, 1984; Schouten *et al.*, 1985). With this mechanism, we might expect that a more concentrated upwelling of the mantle matrix, such as in the form of a plume centered along the ridge segment, would yield a more localized magma reservoir. A highly centered magma reservoir along the ridge segment could make the supply of magma along the ridge more difficult, and therefore yield a progressive, along-axis crustal thinning. Thus, the bulls-eye pattern of the mantle Bouguer anomaly over ridge 4 may represent an intensified signal that combines the effect of a concentrated upwelling instead of a linear upwelling of the hot upper mantle and the effect of progressive, along-axis crustal thinning that may be caused by a very localized magma production zone. We envision an upwelling center that involves the mantle matrix, perhaps similar to the diapiric upwelling suggested by Nicolas and Violette (1982) on the basis of fabrics in ophiolites, rather than the small plumes or blebs of magma described by Schouten *et al.* (1985), which might not have sufficient gravity signature to be directly detectable.

5.2. The off-axis low to the west of ridge 5

To the south of ridge 4, the anomalies show a pattern that is not obviously correlated with the surface RT configuration. The anomalies along ridge 5 are 20 mgal higher than those found at ridges 1 and 2 and they are not the lowest relative to those on both sides of the ridge (Figure 6). Rather, a distinct low is located to the west of ridge 5, and approximately to the north of the western MAR-Meteor intersection. The asymmetry can be seen in the raw data by comparing the FAA and bathymetry on both sides of ridge 5. The FAA on the west side of the ridge at the center of the Bouguer low is 20 to 40 mgal lower than at the comparable position on the east side (Figure 5), even though the seafloor is slightly shallower (Figure 2). Although the mantle Bouguer anomalies also contain the effects of unpredicted variations in crustal structure, the thermal structure beneath ridge 5 is apparently not typical of a normal spreading center. In other words, a mantle thermal model that predicts only age-dependent effects and which is capable of describing the mantle Bouguer anomalies on ridges 1, 2 and 4 will not fully describe the pattern at ridge 5. An off-axis center of upwelling could be responsible for the off-axis low in the mantle Bouguer anomaly. To emphasize deviations from normal oceanic crustal and mantle thermal structures, we compare the observed mantle Bouguer anomalies to those predicted for a simple, 3-D thermal model of the cooling oceanic upper mantle.

6. Mantle Temperature Field

Density variations associated with the temperature structure beneath a RT system are probably the dominant mantle source of Bouguer anomalies. The temperature structure can be predicted on the basis of simple physical models. The primary question in constructing models of the thermal regime of the mantle is the relative importance of flow passively induced by the motions of the plates versus dynamic flow induced by buoyancy effects. We will begin with a purely passive flow model, then discuss features of the gravity field, such as those described in the preceding section, which may indicate the importance of dynamic flow.

In Prince and Forsyth (1988), the gravity effect of the temperature structure was predicted for the MAR-Vema intersection using the thermal model of Forsyth and Wilson (1984) in which the advection of the mantle material is prescribed in both distribution and velocity. In this study, the RT configuration is much more complicated than a single intersection. We employ a more advanced, but still easy-to-implement, model by Phipps Morgan and Forsyth (1988) which features solving for the temperature field of the 3-D viscous flow in the mantle driven by the moving plates on the surface. It is a passive flow model that neglects buoyancy effects and the mechanical thickening of the plates with age, so the type of flow feature that resembles a plume rising beneath the center of a ridge segment and spreading out toward the ends does not develop. In their formulation, the 3-D flow problem for any orthogonal RT configuration can be tackled easily using a 2-D FFT technique. In this region, the major ridges and transforms shown in Figure 1 are described by straight, orthogonal ridges and transforms (Figure 7). The oblique offset at 33.5° S is approximated by several short, en echelon ridges and transforms, and the extensional relay zone in the Cox transform is represented by a short spreading center. In the calculation for viscous flow, we use 256 by 512 points with resolution of about 2 km in both the spreading and along-ridge directions in the horizontal plane for the FFT operation. The edge of the computation area is at least 130 km from spreading centers and 250 km from transform faults, so the implicit periodicity in the FFT algorithm does not affect the main flow pattern. The periodicity only applies to deviations from the average flow pattern for the entire ridge system which is represented by a separate, analytical solution.

Figure 7 is an example of the flow field we calculated at the depth of 9 km beneath the rigid surface. The main features of the 3-D solution that are

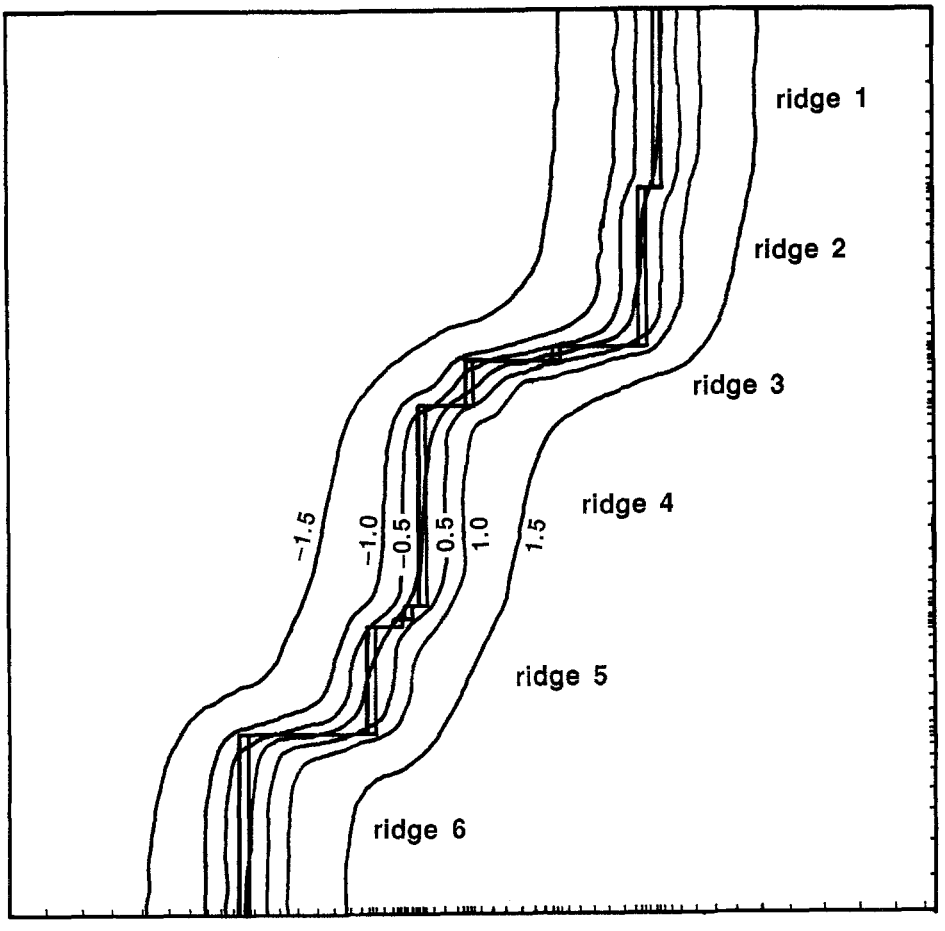

Fig. 7(a).

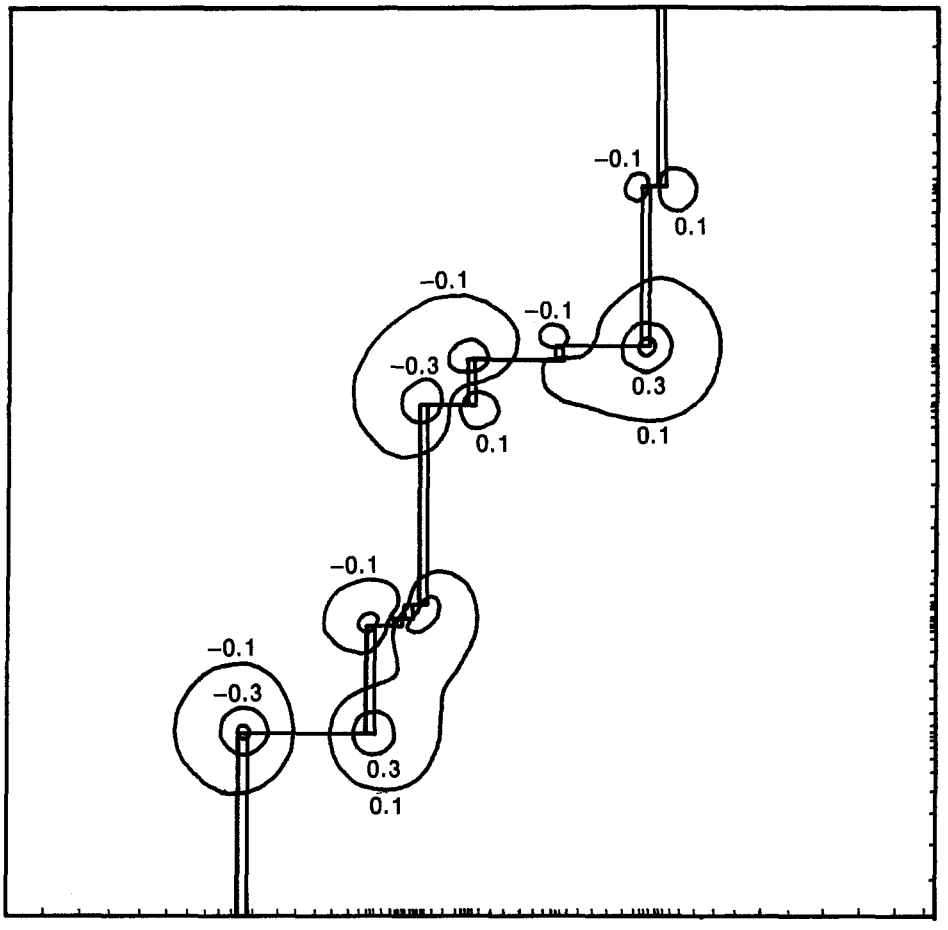

Fig. 7(b).

different from a 2-D flow pattern beneath a ridge of infinite length are the flow across the transform primarily in an oblique direction beneath the RT intersections, indicated by the y-component in Figure 7(b), and induced upwelling at depth that extends beyond the end of a ridge segment beneath the plate on the other side of a transform. The temperature field induced by the 3-D flow in the upper 100 km of the mantle is solved for using finite difference method with conditions of 0 and 1350 degrees on the upper and lower boundaries, respectively, and no horizontal temperature gradient on the four vertical sides of this area. Both 3-D conduction and advection are considered by the finite difference equations, and steady-state flow is assumed. The 3-D grid spacings are variable with minimum of 2 km horizontally near ridge segments and transforms, and 1.5 km vertically near the surface. The temperature field in each discrete horizontal layer defined by the finite difference grids is converted into density variation by multiplying by a thermal expansion coefficient $3.4/(°C \times 10^5)$, and then converted into the gravity signal observed at the sea level employing the FFT technique.

The total gravity signal stacked from all the layers is then rotated and shown in Figure 8 in the same map area as previous data sets. The 3600-m topography contours are superimposed to demonstrate the relationship of the predicted attraction of the mantle thermal structure to the surface RT geometry. There is a total variation of about 50 mgals, 70% of which is contributed from the upper 20 km of the mantle. We only model the effect of the temperature upon the volumetric change of the mantle material. Pressure introduces relatively unimportant horizontal density variations and therefore insignificant gravity anomalies. Since the thermal expansion coefficient is chosen to match the total, average depth change with increasing age, the density anomaly computed from a simple thermal model gives a good first approximation to the total combined effects of thermal

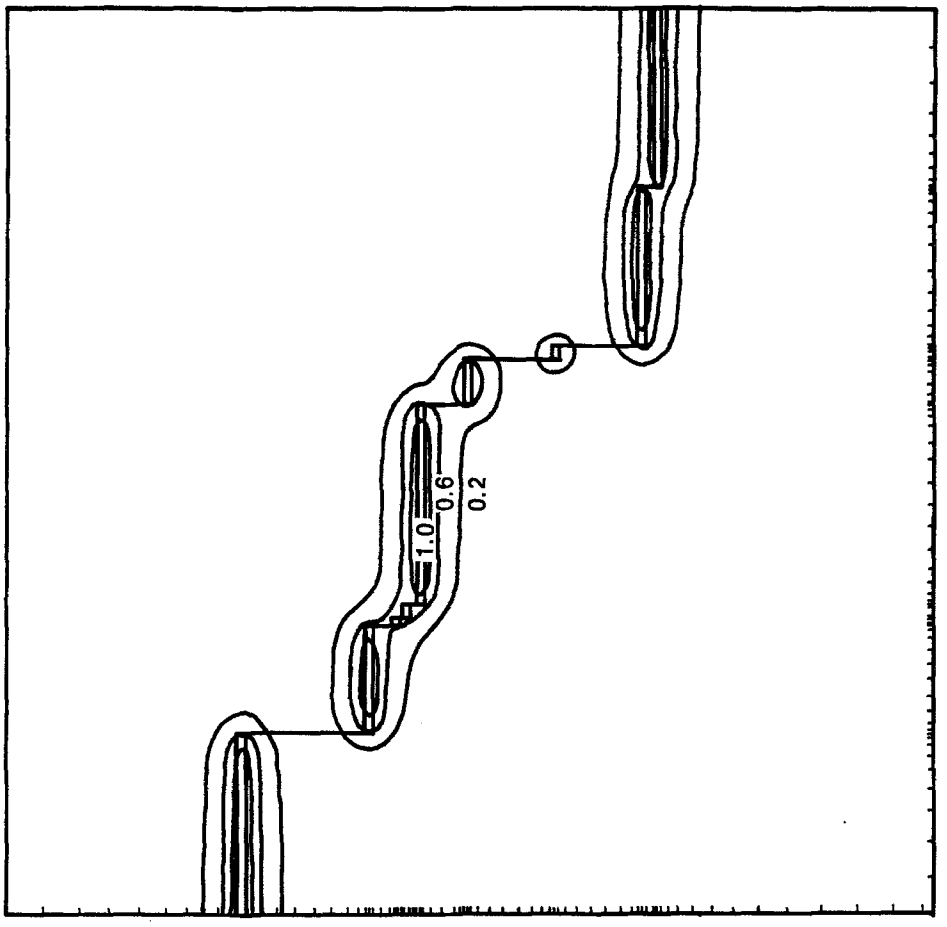

Fig. 7(c).

Fig. 7. Contour maps of the horizontal and vertical components of the 3-D flow field at a depth of 9 km below the rigid plate. In this passive flow model, the surface velocity (half rate of spreading) is prescribed at 1.9 cm yr^{-1}. Contours are labelled in cm yr^{-1}. Double and single straight lines represent ridges and transforms, respectively. Tick marks on the right and bottom margins denote the finite difference grids used to calculate the temperature. (a) Horizontal component of velocity perpendicular to the ridge, positive toward the right. (b) Horizontal component of velocity parallel to the ridge, positive toward the top. (c) Vertical component of velocity, positive toward the surface.

expansion and systematic phase or compositional changes that correlate with temperature or age of seafloor. The primary, unmodelled effects of melt production on the gravity field are thus expected to be related to variations in crustal thickness which represent variations in melt volume delivered to the surface.

While both the theoretical gravity field and the mantle Bouguer anomalies exhibit age-dependent features, there are systematic discrepancies between them. As expected, the suggested off-axis upwelling center to the west of ridge 5 is not predicted by our flow model which is based on the apparent surface RT configuration. Another discrepancy is between the bulls-eye pattern in Figure 6 and the elongate-shaped anomalies in Figure 8 for ridge 4. If the upwelling beneath ridge 4 is in the form of a plume, outward flows from the plume in a radial direction are expected, and dynamic, buoyancy forces may play a more important role in shaping the flow. Obviously, our passive flow model does not predict any circular flow pattern or primary, along-axis flow from the center of ridge 4 (Figure 7). This suggests that the discrepancy could be partly derived from our simplified flow model. However, as discussed in the previous section, a progressive crustal thinning with distance from the center of ridge 4 could also account for the circular pattern in the mantle

Bouguer anomalies. To discriminate between these two possibilities in the future, a flow model incorporating active, dynamic forces and independent knowledge of crustal structure, perhaps from seismic refraction or reflection experiments, are required. To proceed with our 3-D analysis, we use the current passive flow model.

7. Residual Anomalies and Discussion

The theoretical gravity field displayed in Figure 8 is subtracted from the mantle Bouguer anomalies along ship tracks to create the residual anomalies. The residual anomalies are then interpolated into 8 km grids and plotted in Figure 9. The residuals on the grid points range from 23 to 116 mgal with a mean of about 60 mgal. Like the FAA, the residual anomalies are arbitrarily shifted by a constant and the mean can be considered as a zero-level when we discuss the relative magnitude of the anomalies. The peak-to-peak variation has been reduced from the FAA by 34%. Spots with residuals lower than 40 and 30 mgal are located at 33.3° S, 15.3° W and 31.7° S, 14.4° W, which are at the ends of single, isolated tracks and are probably subject to larger errors in the Bouguer correction. Residual anomalies are expected to arise from variations in crustal thickness and density, or from mis-parameterization of the mantle thermal model. We will examine both possibilities in the following sections of interpretations. In Figure 9, the residuals are obviously higher in the southern part of the map than in the northern part. We do not consider this an expression of a possible regional trend in the gravity field, but rather, as we will show, a natural consequence of the variation in crustal thickness and the shift of mantle upwelling centers relative to the surface spreading centers.

To illustrate how much variation in crustal thickness alone would be required to account for the observed residual anomalies in Figure 9, we downward continue the residual anomalies to a depth of 9 km below sea level (average 3 km sea water and 6 km crust) and convert them to crustal thickness shown in Figure 10. These calculations are minimum estimates since the density contrast assumed ($0.6\ \mathrm{Mg\ m^{-3}}$) is greater than the likely density contrast between lower crust and mantle. In this calculation, we remove the mean of 60 mgal from the residuals, cosine-taper the signal with wavelengths, λ, between 35 and 25 km and cut off the signal with wavelengths shorter than 25 km. The resulting variations in crustal thickness thus explain 100% of the anomalies for $\lambda > 35$ km and 0% for $\lambda < 25$ km. In total, 76% of the peak-to-peak variation in the residual anomalies in Figure 9 and more than 95% of the power in the signal is explained by the model shown in Figure 10. The RMS value of the unpredicted anomalies is 4.3 mgal, which is comparable with the RMS value of the crossover errors (4.5 mgal) of the FAA.

7.1. Isostasy at the Cox transform

In most of the Cox transform domain and the surrounding area, the residual anomaly map is nearly featureless. Little horizontal variation in residuals suggests that the crustal thickness is approximately uniform in and near the transform domain as shown in Figure 10. Both the FAA and residuals on some individual tracklines that run through the transform domain are plotted in Figure 11. These profiles confirm that there are no obvious local lows or highs in the half-wavelengths equal to or less than the transform width (10 km). This result is nearly independent of the particular flow or thermal model assumed for the mantle. As can be seen in the mantle Bouguer anomaly (Figure 6), there is no linear anomaly associated with the Cox transform. Subtracting the predicted effects of the thermal model just serves to remove the lows along the spreading center, thus emphasizing the absence of an anomaly associated with the fracture zone. A 2-D numerical experiment (Figure 12) demonstrates that if the 10-km wide Cox transform were locally compensated by thin crust, the mass excess at the bottom of the crust would produce strong Bouguer and residual anomalies at sea level and this predicted signal would also be detected as a significant variation in crustal thickness in a model generated by downward continuation with a wavelength cutoff between 25 and 35 km, as was used in Figure 10. Obviously, Figures 9, 10 and 11 do not show any feature over the Cox transform similar to what is predicted by the Airy model illustrated in Figure 12, indicating that the transform valley is not locally compensated by thin crust.

The apparent, close-to-normal thickness of the crust along the Cox transform inferred from the

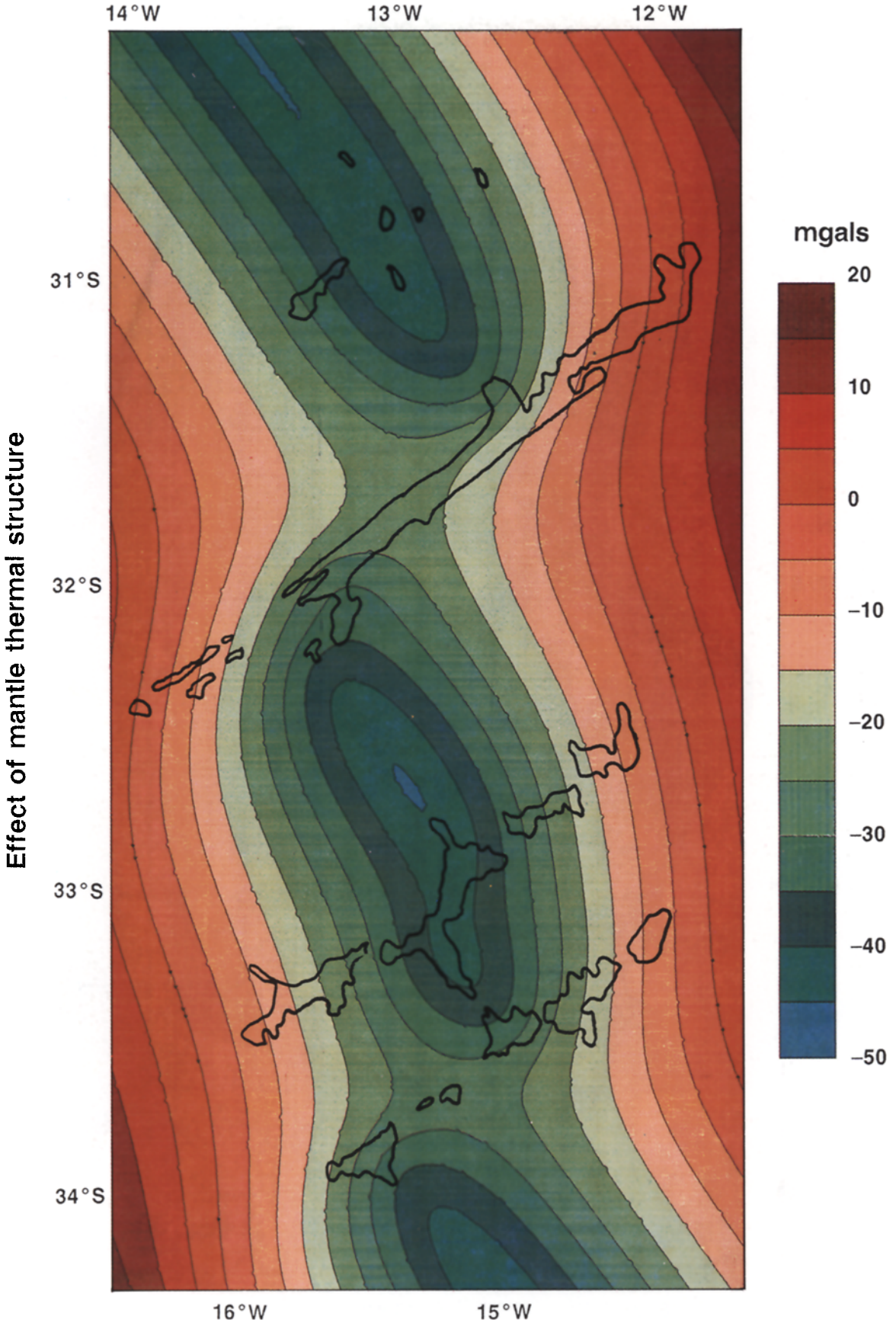

Fig. 8. The predicted mantle Bouguer anomaly from the effect of density anomalies associated with the mantle thermal structure induced by the 3-D flow (illustrated in Figure 7), with 3600-m bathymetric contours superimposed.

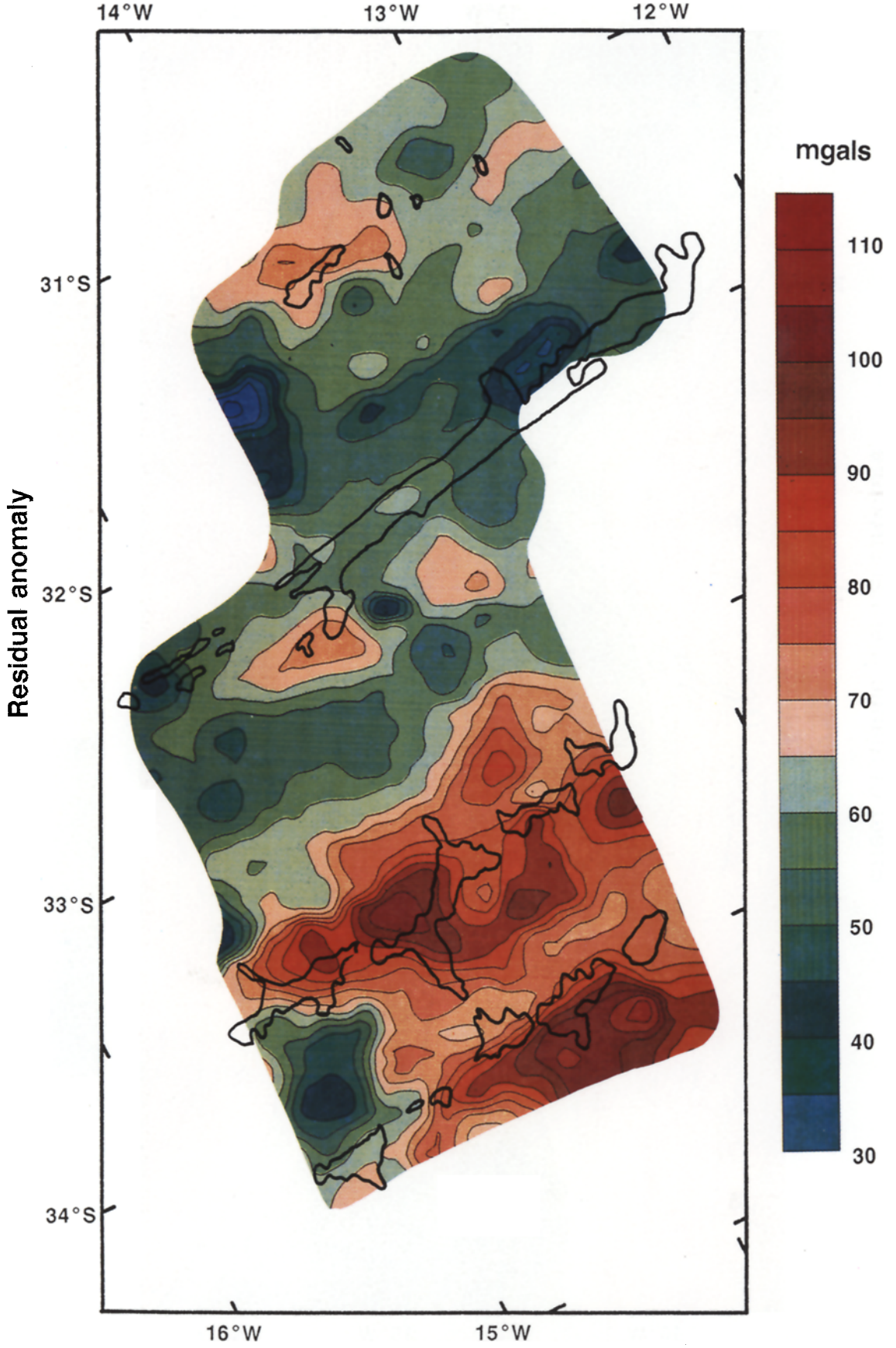

Fig. 9. The residual anomaly map contoured at 5 mgal intervals, with 3600-m bathymetric contours superimposed. Residual anomalies are generated by subtracting the predicted mantle Bouguer anomaly (Figure 8) from the observed anomaly (Figure 6). Anomalies greater than 60 mgal (the mean) can be regarded as high anomalies and those smaller than 60 mgal can be regarded as low anomalies.

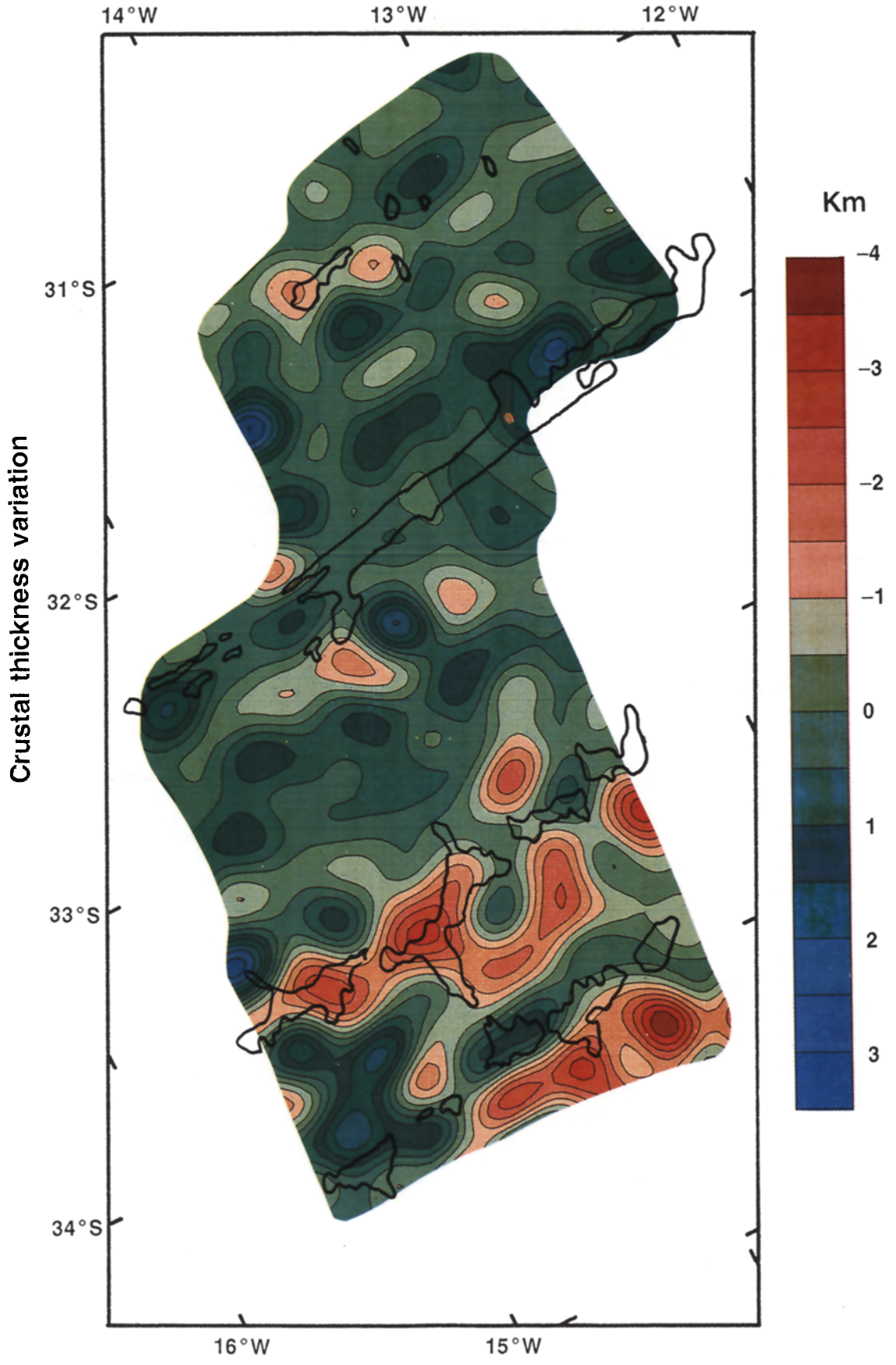

Fig. 10. Variations of crustal thickness determined from downward continuation of residual anomalies (Figure 9) to the base of the crust. Negative and positive values mean crustal thickness thinner and thicker than 6 km, respectively. Gravity signals with wavelength between 25 and 35 km are cosine-tapered, and those with wavelength less than 25 km are eliminated.

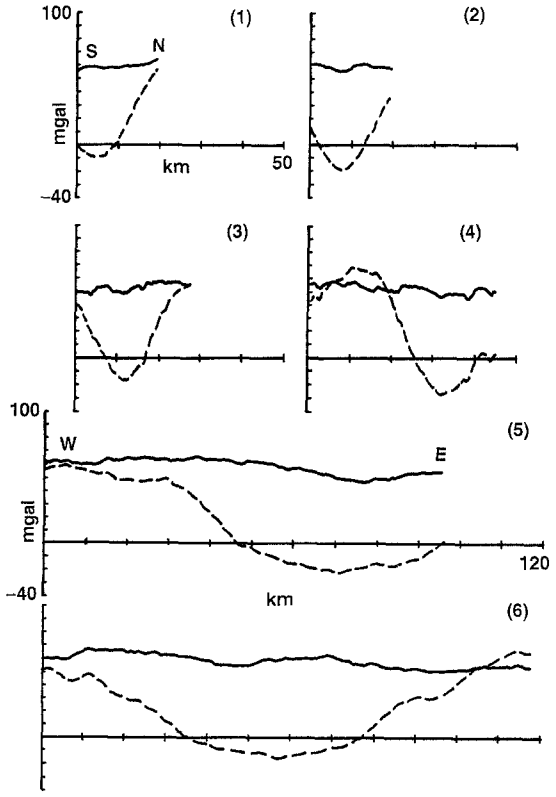

Fig. 11. Free-air anomalies (dashed lines) and residuals (solid lines) on ship tracks that are perpendicular (1–4) and parallel (5, 6) to the Cox transform. Tick mark interval for all profiles is 10 km. The corresponding ship tracks of these profiles are marked by thick lines in Figure 3. These profiles demonstrate that the FAA are almost completely corrected by our 3-D modelling and no obvious residual lows or highs are associated with the transform valley.

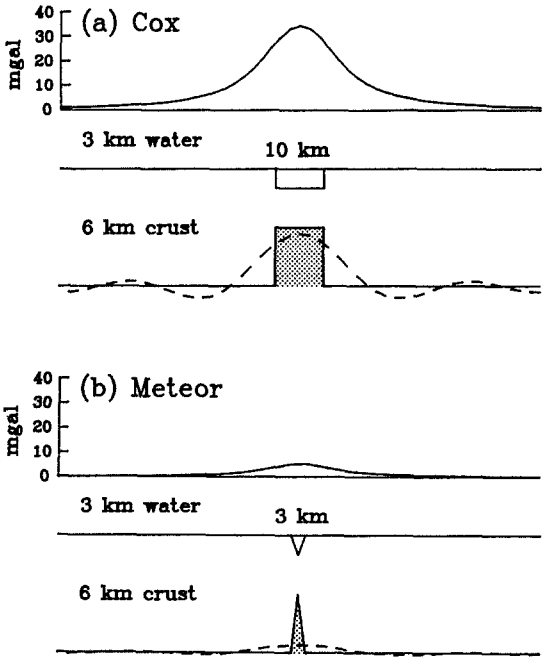

Fig. 12. Hypothetical 2-D Airy models for fracture zone valleys with dimensions similar to those of the (a) Cox transform valley (10 km wide) and (b) Meteor transform valley (3 km wide). Both transform valleys are assumed to be 1 km deep and isostatically compensated by 3 km of crustal thinning. The compensating, excess mass at the bottom of the crust (dotted area) is upward continued to generate the residual anomaly that would be observed at sealevel (solid curves). This predicted residual is then downward continued with cutoff taper between 25 and 35 km to obtain the model of crustal thickness variations (dashed curves). (a) At the Cox transform, a 30–40 mgal anomaly and 2–3 km of crustal thinning are easily distinguishable variations in contrast with the small, observed variation in the residual anomalies (Figures 9 and 11) and the downward-continued crustal thickness (Figure 10). This confirms that the Cox transform valley is not compensated by thin crust in Airy fashion. (b) Expected anomalies from the narrow, active portion of the Meteor transform are too small to unequivocally resolve whether it is underlain by thin crust.

gravity data is not necessarily at odds with the seismic refraction results at some North Atlantic fracture zones. Crust within North Atlantic fracture zones is often found to be thinner than the typical oceanic crust and of unusually low P-wave velocity. Very thin crust (< 3 km) has been observed along the Kane fracture zone (Detrick and Purdy, 1980; Cormier *et al.*, 1984), and crust with more normal thickness of 4–5 km has been found at the Vema (Detrick *et al.*, 1982; Louden *et al.*, 1986), the Oceanographer (Sinha and Louden, 1983) and the Charlie-Gibbs (Whitmarsh and Calvert, 1986) fracture zones. Assuming low velocities correspond to low densities, the anomalous density of the crust may balance the effect of crustal thinning if the crust is only one to two km thinner than normal and decrease the observed gravity anomaly over the fracture zone valley. An analysis of individual profiles crossing the Kane transform demonstrated that there is no evidence in gravity data for systematic crustal thinning beneath the fracture zone valley (Louden and Forsyth, 1982). Abrams *et al.* (1988) report that very low velocities and densities in the upper crust of the Kane fracture zone valley apparently mask the gravity anomaly of the thinned crust which extends beneath both the valley and the flanking transverse ridge. Thus, the absence of an obvious anomaly in gravity could be reconciled with the existence of thin crust if the thin crust has very low density. Isolated areas of thin crust have been inferred in fracture

zones from gravity anomalies, particularly beneath the fracture zone walls, and have been confirmed by seismic refraction experiments (Prince and Forsyth, 1988). In the absence of refraction constraints, the little variation in the residual anomalies across the Cox transform may be interpreted as signature of either a 6 km thick crust of normal density, or somewhat thinner crust with anomalously low density.

It is often proposed that thin crust in fracture zones is caused by restricted magma supply near the end of a ridge axis (e.g., White *et al.*, 1984). Magma supply to the crust might be expected to be reduced if it is supplied by along-axis flow from a magmatic center that is depleted toward the ends of spreading segment, or if melting is reduced in the mantle upwelling beneath the ridge that is in contact with colder mantle beneath the old seafloor across the transform (Fox and Gallo, 1984; Phipps Morgan and Forsyth, 1988). If the crustal structure of the Cox transform is not anomalous, one obvious, possible explanation is that the crustal material is not in short supply in the transform valley. In the Cox transform valley, extra magma could be supplied from the 'extensional relay zone' which behaves more like a spreading center than a pull-apart basin. The extensional relay zone within the Charlie-Gibbs double-transform resembles a short spreading center (50 km long) on morphology and probably produces seafloor typical of that on both sides of the MAR (Searle, 1981). However, this type of accretionary center would also be expected to suffer magma reduction near its end due to the adjacent, cold transform walls. The crust approaching and within the southern transform of the Charlie-Gibbs fracture zone, for example, has been found to be thinned (Whitmarsh and Calvert, 1986). Unless there happened to be an active, dynamic center of mantle upwelling directly beneath the relay zone, it probably would be difficult for this mechanism to generate crust of normal structure in the Cox transform since the magma production along this possible spreading center, that is at most 10 km long, is expected to be greatly influenced by juxtaposing cold slabs on both ends. Nevertheless, in the western, inactive extension of the Cox fracture zone, there is a distinct, ridge-parallel, topographic grain (Fox *et al.*, 1989) similar to that on the seafloor of the Charlie-Gibbs transform, which suggests that the extensional relay zone might have operated like a normal spreading center in the past. As it is difficult with this hypothesis to generate normal crust in the currently active valley of the Cox transform, we examine another alternative hypothesis.

Currently, the active section of the Cox transform valley exhibits no obvious spreading center morphology, but is characterized by broad, deep, deformed basins near the center of the transform. This may favor the explanation that reconciles the seismic and gravity results at other transforms, i.e., a thinner crust of low density. Low density of the fracture zone crust could be due to accumulation of rubble from mass-wasting of the fracture zone walls, extensive cracking, and hydrothermal alteration, primarily serpentinization of the uppermost mantle, which is enhanced by repeatedly opening cracks in the active shear zone (White *et al.*, 1984). It has been suggested that the 4–5 km thick crust beneath the principal transform deformation zone (PTDZ) of the Vema transform consists of a thin, basaltic crust and a serpentinized ultramafic layer (Detrick *et al.*, 1982; Louden *et al.*, 1986). Hydrothermal circulation in the Cox transform could be extensive and intensive through the highly fractured valley floor rather than confined only in the PTDZ so that gravity detects an apparently normal crustal thickness in the entire transform domain.

Whatever the explanation, with a density structure equivalent to having a 6 km thick crust, the deep valley of the Cox transform must be kept at its level by large stresses in the lithosphere and/or dynamic forces in the mantle. It is not intuitively obvious what mechanism is operating to form or hold such a long, 10 km wide strip of topography 1–2 km lower than its surrounding area. In view of the straight boundaries of the transform which sharply separate the valley and the outside 'normal' seafloor, the transform valley resembles a graben more than the downwarping of an elastic plate. One of the possible explanations for the lack of equilibrium of the transform valley comes from the combination of the concepts of serpentinization described above and 'freezing-in' of topography (Prince and Forsyth, 1988). The crust may be initially thin and isostatically adjusted at a deep level when it was formed. Subsequent cooling and fracturing in the transform valley leads to extensive hydrothermal circulation which serpentinizes the upper mantle and 'thickens'

the crust. If the lithosphere has cooled and developed high rigidity before or during the serpentinization, the thickened crust may not be able to rebound to its equilibrium level and will be 'frozen-in' as a deep valley as the transform evolves. In order for this mechanism to be effective, at least one of the steep walls of the transform must not be a weak, active fault that would allow decoupling of the valley floor from the surrounding plate.

7.2. The Meteor Transform

There are two levels of residual anomalies along the Meteor transform and its eastern inactive extension (Figure 9). The residuals are about 60 to 70 mgal on the western half of the active transform, and more than 80 mgal on the eastern half of the transform and the eastern inactive fracture zone. The transition between these two levels does not occur at the eastern MAR-Meteor intersection, so it cannot be explained as being related to the interaction of the transform with ridge segment 5. The 60–70 mgal residuals are close to the average (60 mgal) of this data set, but the residuals along the eastern inactive fracture zone are well above average. This suggests that thin crust is present beneath the widened fracture zone trough (Figure 10) but not present, or not detectable, beneath the extremely narrow, active transform valley (Figure 12). If the effective elastic thickness of the plate is several km as has been suggested for young sea floor in the Atlantic (Cochran, 1979; Louden and Forsyth, 1982), the stresses required to maintain this narrow feature out of isostatic equillibrium could easily be supported within the lithosphere. It is interesting to note that the highest residual is not over the deepest part of the fracture zone trough but actually over the southern wall of the fracture zone, a feature similar to what has been found at the Vema transform (Prince and Forsyth, 1988). In fact, the fracture zone resembles a transition between low residual anomalies to the north and higher anomalies to the south, possibly marking a difference in thickness of crust produced at spreading centers 5 and 6, more than it does a site of anomalous crust. Although we have relatively little constraint to the south of the Meteor fracture zone, there is a suggestion that thin crust extends 30 km or more to the south. An alternative explanation of this large region of positive residual anomalies is that it is one of the effects of centers of upwelling, particularly possible off-axis upwelling.

7.3. Ridge Segment 5 and Off-Axis Upwelling

The residual anomalies to the north of the Meteor transform are lower on the west side (40–60 mgal) than on the east side (70–80 mgal) of ridge 5 (Figure 9). The distinct local low on the west side of ridge 5 and to the north of the western Meteor-MAR intersection presented in the mantle Bouguer anomaly (Figure 6) remains in the residual anomaly.

The asymmetry in residual anomaly about ridge 5 could be caused by several possible mechanisms. First, the crust to the east could be generally 1–2 km thinner than the crust to the west (Figure 10). Ridge 5 has spread asymmetrically in the past 4 m.y. with faster accretion on the west side than on the east (Welch *et al.* 1987; see discussion in the section of morphology of ridge-transform system). Although we cannot rule out the possibility of variations in crustal thickness, if approximately the same volume of magma is delivered to both sides of the spreading center, the faster (west) side might be expected to have thinner crust than the slower (east) side, which is opposite to the sense of the observed gravity anomalies. A second possibility is that the slower spreading toward the east could make the mantle on the east side colder and denser than the mantle on the west side at the same distance from the spreading center. Our thermal model (Figures 7 and 8) assumes symmetric spreading, so we might expect higher residuals to the east and lower residuals to the west. Although the observed anomaly on the faster side is lower, asymmetric spreading should produce a Bouguer anomaly that increases monotonically with distance from the spreading center, which is obviously incompatible with the observed mantle Bouguer anomalies across ridge 5 that reach a minimum 50 km to the west of the spreading center (Figure 6). Third, as suggested by the pattern of the mantle Bouguer anomalies, the thermal regime underneath ridge 5 could be anomalous. The circular, local low in the mantle Bouguer and residual anomalies to the west of ridge 5 may represent a low density body in the mantle. The maximum depth to the center of this low density body can be estimated using the point source solution which has a characteristic 35% fall-off at a horizontal distance equal to the depth of the source. The 35% fall-off distance of

the observed local low is about 30 km, which implies that the source of the anomaly could be anomalous temperatures in the mantle distributed vertically in much the same way as beneath a ridge segment in the passive flow model. A low density source in the mantle is thus likely to be a center of upwelling that is similar to one beneath a spreading center. The greater depth of the median valley for ridge 5 than for others could be an indicator of the difficulty of supplying magma to a spreading center from an off-axis upwelling. Although the seafloor at the site of the Bouguer low is a few hundred meters shallower than at the comparable position on the other side of ridge 5, the expected topographic anomaly for this off-axis upwelling may not be as obvious as at a ridge axis due to higher rigidity of the lithosphere. Future seismic refraction or multi-channel reflection experiments should be able to distinguish whether the anomaly is of crustal or mantle origin.

Under little observational constraint, we speculate about the possibilities for the origin of an off-axis upwelling center and the associated shallow thermal anomaly that could produce the observed mantle Bouguer anomalies. We describe three possible scenarios below.

7.3.1. *Scenario 1: Asymmetric Spreading*

One possibility is that the ridge segment and associated upwelling center were coincident with this local gravity low in the past. By asymmetric spreading, ridge segment 5 could have moved eastward to its current position while the upwelling center remained at its previous spot which is now to the west of ridge 5 (Figure 13a). To move the surface ridge segment eastward by about 50 km, asymmetric spreading on ridge 5 would have to have operated at current rate for 30 to 40 m.y. Longer, off-axis, magnetic anomaly profiles could resolve whether the amount of asymmetric spreading required actually occurred. Although this model adequately takes advantage of the actual sense of asymmetric spreading on ridge 5, the major problem is that the off-axis upwelling has to persist and be active at this spot for tens of m.y. to supply magma to a ridge that has migrated 50 km to the east.

7.3.2. *Scenario 2: Flow away from the Tristan da Cunha Hotspot*

Another possibility is motivated by the observations that the local gravity low is located just to the north of the western intersection of the Meteor transform and the MAR and that there is another similar, but less well-constrained, low north of the western intersection of the Cox transform and the MAR (Figures 6 and 9). In the past, the Meteor transform could have been to the north of this hot plume which was once an upwelling center beneath ridge segment 6 (Figure 13b). If upwelling centers tend to remain fixed within the asthenosphere, then sublithospheric flow northward away from the Tristan da Cunha hotspot (at about 37 to 38° S) could have swept the upwelling center across the transform to its current suggested position. Nicolas *et al.* (1988) report evidence for a similar geometry in the Oman ophiolite. Based on fabrics in harzburgites, they suggest that there were several upwelling mantle diapirs in line with a ridge segment, but, there were other diapirs separated from the ridge segment by about 50 km. In our study area, we might also expect other upwelling centers to have moved with respect to the plates, perhaps leaving evidence at the surface in the form of aseismic bathymetric highs that in plan view are northward pointing V-shapes (Figure 13b). There is some suggestion of forms of this type leading away from the highs on ridge segments 2 and 4 (Figure 2), but off-axis coverage is not sufficiently dense to establish their existence. Geochemical variations in basalts suggest extensive mixing, and thus northward flow, of an enriched component from the Tristan da Cunha mantle plume with depleted, normal mid-ocean ridge basalts (N-type MORBs) at far north as 31° S (Schilling *et al.*, 1985; Humphris *et al.*, 1985).

7.3.3. *Scenario 3: Deep Smoothing of Ridge Trend.*

A very preliminary calculation of three dimensional convection beneath ridge systems with transform faults indicates that the dynamic component of convection tends to produce upwelling with a geographic pattern that emphasizes the longest wavelength components of the surface ridge-transform geometry. This means that the pattern of dynamic upwelling at depth has difficulty 'following' all the kinks and jogs at the surface, producing a smoothed trend of the upwelling region (Figure 13c). If there is broad, smooth upwelling at depth, local instabilities could arise within the upwelling region producing apparently isolated upwelling centers that can be detected with gravity measurements that are most sensitive to

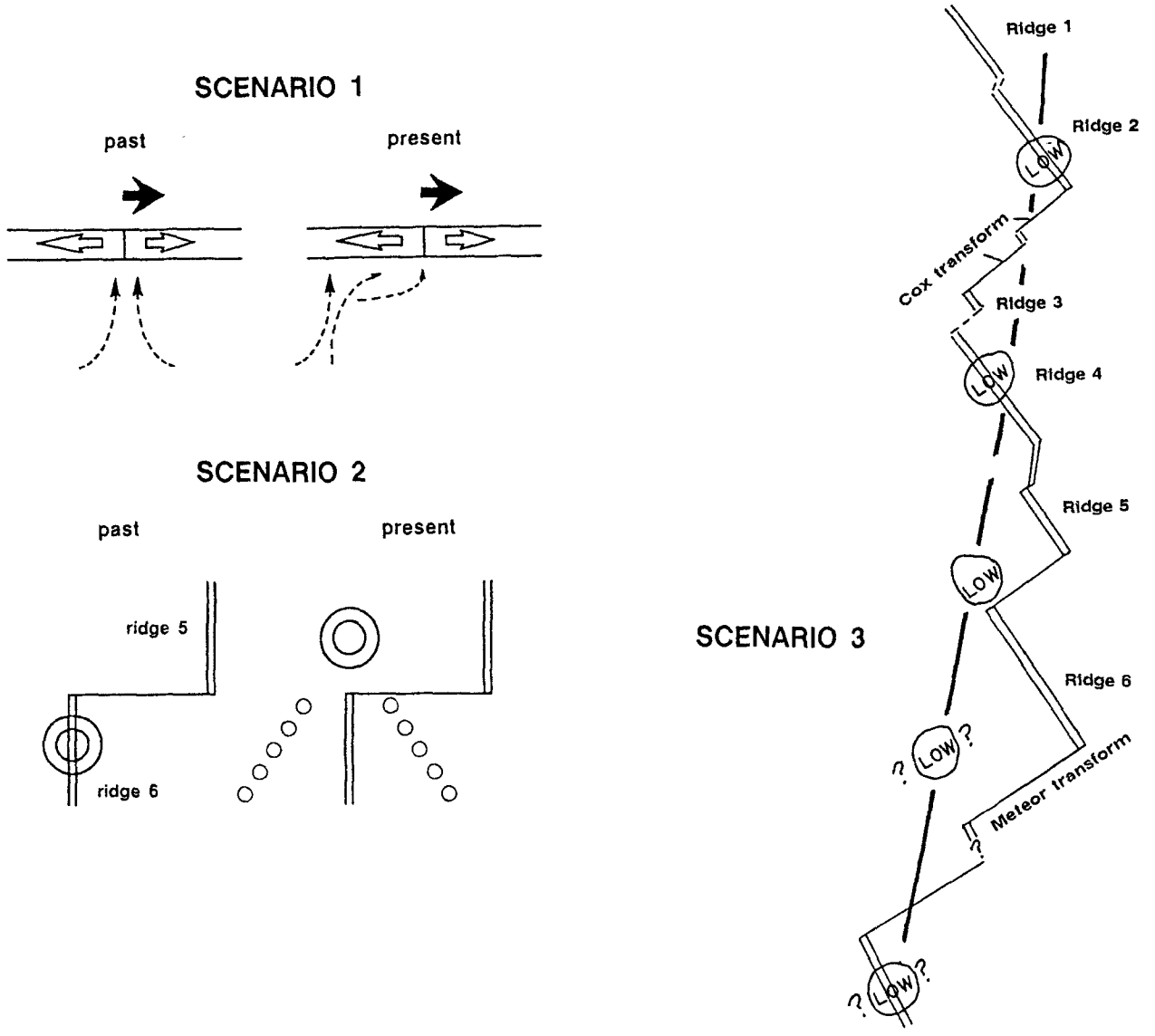

Fig. 13. Schematic diagrams illustrating three possible scenarios for the development of the suggested upwelling center to the west of ridge 5. (a) Scenario 1; vertical cross section perpendicular to ridge 5. Dashed lines with arrows represent upwelling in the upper mantle. Upwelling center is originally beneath ridge 5, but remains behind as ridge migrates to east through asymmetric spreading. (b) Scenario 2; map view. Upwelling center (double circle) is originally beneath ridge 6, but asthenospheric flow away from the Tristan da Cunha hot spot sweeps it north of the Meteor transform to its present position to the west of ridge 5. Single circles forming a truncated V represent the possible topographic signature of the northward-moving upwelling center created while it was beneath ridge 6. (c) Scenario 3; map view of the extended area including all of ridge 6, which terminates to the south at a double transform offsetting the spreading centers in a right lateral sense by about 150 km. This transform has not been surveyed in detail, so the position of the extensional relay zone is questionable. The dark line represents the general trend of the deep, dynamic upwelling that follows the long-wavelength geometry of the surface plate boundary. Patches labelled 'low' are individual upwelling centers near surface that are detected by gravity lows. If these occur at regular intervals, we might expect additional centers at the sites indicated by question marks.

near-surface structure. Ridge 6 is about 120 km long, with another large, right-lateral transform beginning at its southern end. As suggested in Figure 13c, the off-axis Bouguer low to the west of ridge 5, the bulls-eye low on ridge 4, and the low on ridge 2 form a roughly linear trend (Figures 6 and 13c), which may reflect the average trend of the ridge axis in the region. In this scenario, we would predict that there will also be an off-axis low west of ridge 6, and that the poorly resolved low north of ridges 3 and 4 (Figures 6 and 9) will prove to be an artifact of poor data at the end of ship tracks. A westerly-shifted

upwelling center for ridge 6 will partially explain the strong positive residuals south of the Meteor transform and its eastern extension (Figure 9). One recent observation which may possibly support this scenario of smoothing of the overall ridge geometry is the remarkably straight alignment of maxima in the roughness of the geoid in the South Atlantic which passes through the more irregular plate boundary (Gibert and Courtillot, 1988).

7.4. Crustal thinning at the oblique offset and other discordant zones

There are significant, high residual anomalies (> 80 mgal compared with the mean of 60 mgal) distributed in the vicinity of the oblique, deep basin that connects ridge 4 to the north and ridge 5 to the south at about 33.5° S. The 80 mgal contour is roughly elliptical with long axis subparallel to the fracture zone trace of this oblique offset (Figure 9). If the mantle thermal regime beneath this oblique offset has been modelled correctly, a minimum of 1–3 km crustal thinning as suggested in Figure 10 is needed to explain the observed residual variations.

In many ways this oblique basin represents an unusual tectonic element in the RT system. For example, it connects one ridge segment with an axial bulge and another ridge segment with a deep rift valley (Figure 2). As discussed earlier, this offset has evolved from a fracture zone, and currently may represent an oblique spreading center where opening and perhaps stretching of the seafloor occur. It should be noted in Figure 10 that the thin crust is primarily distributed to the north of the western fracture zone trace and to the south of the eastern fracture zone trace (these two traces are not precisely aligned), and in a band that covers the seafloor created by the oblique spreading center. Although we do not know the dynamics that shape this oblique offset, we suggest that thin crust is likely to be generated in this oblique spreading center due to restricted melt generation and crustal stretching. If magma is supplied by along-axis flow from upwelling centers, it could be cut off by a small offset in the spreading center. In an oblique spreading center, unlike in transform faults, we may see manifested in the gravity data the full effect of crustal thinning, because the magma starved zone is broader and the crust may not experience the intense fracturing and alteration present in a shear zone. Note that, although the overall trend of the trace of the oblique offset is parallel to the Cox and Meteor transforms, there is very little small-scale, transform-parallel topography present (Figure 2). This may indicate that intense shearing after formation of the seafloor does not occur. Instead, the seafloor morphology is hummocky, with many small highs and basins, suggesting dismemberment and rotation of large blocks rather than pervasive, small-scale deformation.

As shown in Figure 10, the thin crust on either side of the ridge extends to a distance of 80 km or more from the ridge. This implies that the oblique basin might have formed at least 4 Ma when the offset was approximately 10 km longer than the current offset of 25 km. We can therefore exclude the shortening of the offset in the latest phase of asymmetric spreading as a cause of the oblique geometry of the offset. Because the mantle thermal structure beneath ridge 5 may be anomalous as described in the previous section, the thermal structure beneath the oblique offset could be affected and, therefore, predicted inadequately by our passive, viscous flow model. Although the actual flow pattern and its impact on the temperature field of the mantle is not known, we expect that ignoring the possible displacement of the upwelling center to the west of ridge 5 could cause an underestimate of the crustal thinning to the west of the oblique offset and an overestimate of the crustal thinning to the east of the oblique offset. This bias is not likely to cause the pattern shown in Figures 9 and 10, as it is difficult to explain by this mechanism the relatively narrow zone of pronounced positive anomalies. We believe that the effect of thin crust overpowers the signal from the possible unmodelled mantle thermal structure along the fracture zone traces of the oblique offset, and the inferred area of thin crust is to the first order correct.

At two other smaller offsets, slightly high residuals also indicate thin crust. A patch of 70 mgal anomalies, contrasting with the surrounding 60 mgal, are around the northern offset at 31.3° S, and a similar 70 mgal closed contour is shown at the offset south of the Cox transform at 32.5° S (Figure 9). The downward continuation map shows that 1–2 km of crustal thinning occurs along these two offset traces relative to the surrounding area (Figure 10). Thin crust has also been found from seismic data along small-offset fracture zones in the North Atlantic (Mutter and Detrick, 1984; White *et al.*, 1984).

Since the age contrast is small across the small offsets, the effect of juxtaposing of a cold slab next to a spreading segment may not be an important factor in reducing the magma production near the end of a spreading segment. Thin crust along the small-offset fracture zones favors models in which magma is primarily supplied laterally from the center of the ridge segment, as opposed to models in which magma is supplied from beneath the entire segment (White *et al.*, 1984; Whitehead *et al.*, 1984; Schouten *et al.*, 1985).

7.5. Isostasy of ridge segments

Assuming constant crustal thickness leaves no obvious residual variations across the rift valleys of any of the ridge segments (Figure 9), indicating that the greater depth of median valleys is not compensated by thin crust or by shallow density anomalies in the mantle. This is consistent with the results from gravity analyses for the rift valleys of the northern MAR (Watts, 1982; Parmentier and Forsyth, 1985; Dalloubeix *et al.*, 1988; Prince and Forsyth, 1988), and the seismic refraction study along the MAR median valley south of the Kane transform (Purdy and Detrick, 1986). Dynamic forces and stresses in the lithosphere are thought to be responsible for the topography of rift valleys (e.g., Lachenbruch, 1973; Phipps Morgan *et al.*, 1987). Although there is no local compensation of the narrow median valleys, the positive correlation of the depth of the median valley in each segment with the mantle Bouguer anomaly suggests that there is either regional compensation within the mantle or that the mantle thermal state controls the expression of the dynamic processes. There is no similar correlation of the elevation of the flanking walls of the valleys with the mantle Bouguer anomaly. In fact, if anything, the correlation is reversed. This suggests that changes in the depth of the median valley do not represent a straightforward isostatic response to the thermal structure, but rather an indirect effect of the thermal structure on the rate of thickening of the lithosphere, which is thought to be the primary factor controlling the dynamic formation of the median valley (Lachenbruch, 1973; Phipps Morgan *et al.*, 1987).

Although the crustal thickness is inferred to be uniform across the shallow portion of ridge 4, the mechanism of isostasy here may be different from that of other ridge segments. We calculated the topography across a spreading center due to pure thermal expansion using our thermal model and compared it with the observed profiles. It is not surprising that, owing to its shallow, uplifted ridge axis, the topographic profile across the center of ridge 4 mimics the theoretical one much better than those across other segments. This indicates that the middle portion of ridge 4, in contrast to typical slow spreading axes, could be more directly compensated by the mantle thermal structure, and the indirect, dynamic response of the lithosphere may not be as important. Along the strike of ridge 4, the median valley deepens toward both ends of the ridge segment. The general deepening of the sea floor toward the ends may be compensated by the suggested progressive crustal thinning, and/or cooling of the upper mantle as it flows along-axis from a central upwelling plume. But, again, the relief of the axis relative to the valley walls is not compensated at shallow depths, so the deepening of the median valley must be a primarily dynamic feature.

8. Conclusions

3-D gravity analysis of the southern MAR between 31 and 34.5° S reveals that the major short-wavelength, topographic features, i.e., the transform faults and median valleys, are not isostatically compensated by thin crust. The wide fracture zone valley east of the Meteor transform could be underlain by thin crust. Low density rubble from mass wasting, fracturing, and hydrothermal alteration of the uppermost mantle may be responsible for the apparent, normal thickness of the crust along the Cox transform valley inferred from the gravity data. Crust that is 1–3 km thinner than normal might have been generated from the oblique offset at 33.5° S in the past 4 m.y. Two other small-offset fracture zones are also underlain by thin crust, but less pronounced than that in the vicinity of the 33.5° S oblique offset. Dynamic processes controlled by the thermal state of the mantle are probably responsible for lack of isostasy of the median valleys.

The mantle Bouguer anomaly has proven to be effective in illuminating the thermal structure of the mantle and patterns of variations in crustal thickness. The major question is the nature of flow in the mantle. Is a simple model of flow passively driven by the motions of the plates adequate, or are dynamic,

buoyancy forces leading to centers of upwelling important? The geographic pattern of anomalies suggests to us that the dynamic effects are probably important for some ridge segments. Upwelling beneath the longest ridge segment in this area may be more in the form of a plume, rather than the linear upwelling predicted by a passive flow model. A progressive crustal thinning along-axis may be associated with upwelling of this fashion. The upwelling center in the mantle for the ridge to the south of the oblique offset is probably off-axis, being 50 km to the west of this ridge.

Acknowledgments

We thank Jeff Fox, Nancy Grindlay, Ken Macdonald, and Stuart Smith for providing their data prior to publication, and the Captain and crew of the R/V *Thomas Washington* for their support at sea. We also thank Clyde Nishimura for providing improved Navigation and SeaBeam data. Color figures were generated at the SeaBeam group of URI with the help of Robert Pochalny; we are grateful to him. This research was supported by the Office of Naval Research under contract N00014-85-K-0515.

References

Abrams, L. J., Detrick, R. S., and Fox, P. J., 1988, Morphology and Crustal Structure of the Kane Fracture Zone Transverse Ridge, *J. Geophys. Res.* **93**, 3195–3210.

Briggs, I. C., 1974, Machine Contouring Using Minimum Curvature, *Geophysics* **39**, 39–48.

Cochran, J. R., 1979, An Analysis of Isostasy in the World's Oceans: 2. Midocean Ridge Crests, *J. Geophys. Res.* **84**, 4713–4729.

Cormier, M. H., Detrick, R. S., and Purdy, G. M., 1984, Anomalously Thin Crust in Oceanic Fracture Zones: New Seismic Constraints from the Kane Fracture Zone, *J. Geophys. Res.* **89**, 10249–10266.

Crane, K., 1976, The Intersection of the Siqueiros Transform Fault and the East Pacific Rise, *Mar. Geol.* **21**, 25–46.

Dalloubeix, C., Fleitout, L., and Diament, M., 1988, A New Analysis of Gravity and Topography Data over the Mid-Atlantic Ridge: Non-Compensation of the Axial Valley. *Earth, Planet, Sci. Lett.* **88**, 308–320.

Detrick, R. S. and Purdy G. M., 1980, The Structure of the Kane Fracture Zone from Seismic Refraction Studies, *J. Geophys. Res.* **85**, 3759–3778.

Detrick, R. S., Cormier, M. H., Prince, R. A., Forsyth, D. W., and Ambos, E. L., 1982, Seismic Constraints on the Crustal Structure within the Vema Fracture Zone, *J. Geophys. Res.* **87**, 599–610.

Forsyth, D. W. and Wilson, B., 1984, Three-Dimensional Temperature Structure of a Ridge-Transform-Ridge System, *Earth Planet. Sci. Lett.* **70**, 355–362.

Fox, P. J. and Gallo, D. G., 1984, A Tectonic Model for Ridge-Transform-Ridge Plate Boundary: Implications for the Structure of Oceanic Lithosphere, *Tectonophysics* **104**, 205–242.

Fox, P. J., Grindlay, N., Macdonald, K. C., Welch, S. M., Forsyth, D. W., and Kuo, B. Y., 1989, Mid-Atlantic Ridge (31° S–34° S): Temporal and Spatial Variations of Accretionary Processes, *Mar. Geophys. Res.* (in press).

Gibert, D. and Courtillot, V., 1988, Geoid Roughness and Long-Wavelength Segmentation of the South Atlantic Spreading Ridge, *Nature* **333**, 255–258.

Humphris, S. E., Thompson, G., Schilling, J.-G., and Kingsley, R. H., 1985, Petrological and Geochemical Variations along the Mid-Atlantic Ridge between 46° S and 32° S: Influence of the Tristan da Cunha Mantle Plume, *Geochim. Cosmochim.* **49**, 1445–1464.

Lachenbruch, A. H., 1973, A Simple Mechanical Model for Oceanic Spreading Centers, *J. Geophys. Res.* **78**, 3395–3417.

Louden, K. E. and Forsyth, D. W., 1982, Crustal Structure and Isostatic Compensation near the Kane Fracture Zone from Topography and Gravity Measurements-1. Spectral Analysis Approach, *Geophys. J. Roy. Astron. Soc.* **68**, 725–750.

Louden, K. E., White, R. S., Potts, C. G., and Forsyth, D. W., 1986, Structure and Seismotectonics of the Vema Fracture Zone, Atlantic Ocean, *J. Geol. Soc. Lond.* **143**, 795–805.

Macdonald, K. C., Kastens, K., Spiess, F. N., and Miller, S. P., 1979, Deep Tow Studies of the Tamayo Transform Fault, *Mar. Geophys. Res.* **4**, 37–70.

Mutter, J. C. and Detrick, R. S., 1984, Multichannel Seismic Evidence for anomalously Thin Crust at Blake Spur Fracture Zone, *Geology*, **12**, 534–537.

Nicolas, A. and Violette, J. F., 1982, Mantle Flow at Oceanic Spreading Centers: Models Derived from Ophiolites, *Tectonophys.* **81**, 319–339.

Nicolas, A., Boudier, F., and Ceuleneer, G., 1988, Mantle Flow Patterns and Magma Chambers at Ocean Ridges: Evidence from the Oman Ophiolite, *Mar. Geophys. Res.* **9**, 293.

Nishimura, C. E. and Forsyth, D. W., 1988, Improvements in Navigation using SeaBeam Crossing Errors, *Mar. Geophys. Res.* **9**, 333.

Parker, R. L., 1972, The Rapid Calculation of Potential Anomalies, *Geophys. J. Roy. Astron. Soc.* **31**, 447–455.

Parmentier, E. M. and Forsyth, D. W., 1985, Three-Dimensional Flow beneath a Slow Spreading Ridge Axis: a Dynamic Contribution to Deepening of the Median Valley toward Fracture Zones, *J. Geophys. Res.* **90**, 678–684.

Phipps Morgan, J. and Forsyth, D. W., 1988, 3-D Flow and Temperature Perturbations due to a Transform Offset: Effects on Oceanic Crustal and Upper Mantle Structure, *J. Geophys. Res.* **93**, 2955–2966.

Phipps Morgan, J., Parmentier, E. M., and Lin, J., 1987, Mechanisms for the Origin of Mid-Ocean Ridge Axial Topography: Implications for the Thermal and Mechanical Structure of Accreting Plate Boundaries, *J. Geophys. Res.* **92**, 12823–12836.

Pochalny, R. A., Detrick, R. S., and Fox, P. J., 1988, Morphology and Tectonics of the Kane Transform from SeaBeam Bathymetry Data, *J. Geophys. Res.* **93**, 3179–3194.

Prince, R. A. and Forsyth, D. W., 1984, A Simple Objective Method for Minimizing Crossover Errors in Marine Gravity Data, *Geophysics*, **49**, 1070–1083.

Prince, R. A. and Forsyth, D. W., 1988, Horizontal Extent of Anomalously Thin Crust near the Vema Fracture Zone from

the Three-Dimensional Analysis of Gravity Anomalies, *J. Geophys. Res.*, **93**, 8051–8063.

Prothero, W. A. Jr. and Reid, I. D., 1982, Microearthquakes on the East Pacific Rise at 21° N and the Rivera Fracture Zone, *J. Geophys. Res.* **87**, 8509–8518.

Purdy, G. M. and Detrick, R. S., 1986, Crustal Structure of the Mid-Atlantic Ridge at 23° N from Seismic Refraction Studies, *J. Geophys. Res.* **91**, 3739–3762.

Schilling, J. G., Thompson, G., Kingsley, R., and Humphris, S., 1985, Hotspot-Migrating Ridge Interaction in the South Atlantic, *Nature* **313**, 187–191.

Schouten, H., Klitgord, K. D., and Whitehead, J. A., 1985, Segmentation of Mid-Ocean Ridges, *Nature* **317**, 225–229.

Searle, R., 1981, The Active Part of Charlie-Gibbs Fracture Zone: a Study Using Sonar and Other Geophysical Techniques, *J. Geophys. Res.* **86**, 243–262.

Sinha, M. C. and Louden, K. E., 1983, The Oceanographer Fracture Zone-1, Crustal Structure from Seismic Refraction Studies, *Geophys. J. Roy. Astron. Soc.* **75**, 713–736.

Sleep, N. H., 1969, Sensitivity of Heat Flow and Gravity to the Mechanism of Seafloor Spreading, *J. Geophys. Res.* **74**, 542–549.

Spudich, P. and Orcutt, J., 1980, A New Look at the Seismic Velocity Structure of the Oceanic Crust, *Rev. Geophys. and Space Phys.* **18**, 627–645.

Talwani, M., 1966, Some Recent Developments in Gravity Measurements Aboard Surface Ships, in H. Orlin, (ed.), *Gravity Anomalies; Unsurveyed Areas, Geophys. Monogr., 9*, AGU, Washington, D.C., pp. 31–47.

Trehu, A. M. and Solomon S. C., 1983, Earthquakes in the Orozco Transform Zone: Seismicity, Source Mechanisms, and Tectonics, *J. Geophys. Res.* **88**, 8203–8225.

Watts, A. B., 1982, Anomalies over Oceanic Rifts, in G. Palmason, (ed.), Continental and Oceanic Rifts. Geodyn. Ser., 8, AGU, Washington, D. C., pp. 99–105.

Weissel, P. and Watts, A. B., 1988, On the Accuracy of Marine Gravity Measurements, *J. Geophys. Res.* **93**, 393–414.

Welch, S. M., Macdonald, K. C., Miller, S. P., Fox, P. J., and Grindlay, N., 1987, Magnetic Analysis of a Slow Spreading Plate Boundary in the South Atlantic (abstract), *EOS* **67**, 44.

White, R. S., Detrick, R. S., Sinha, M. C., and Cormier, M. H., 1984, Anomalous Seismic Crustal Structure of Oceanic Fracture Zones, *Geophys. J. Roy. Astron. Soc.* **79**, 779–798.

Whitehead, J. A., Dick, H. B., and Schouten, H., 1984, A Mechanism for Magmatic Accretion under Spreading Centers, *Nature* **312**, 146–148.

Whitemarsh, R. B. and Calvert, A. J., 1986, Crustal Structure of Atlantic Fracture Zones-1. The Charlie-Gibbs Fracture Zone, *Geophys. J. Roy. Astron. Soc.* **85**, 107–138.